Investigation of Inorganic Self-healing of Municipal Waste Concrete with Steel Fibers exposed to Elevated Temperature

Thesis submitted in partial fulfillment of the requirements for the degree of Master of Science in

Civil Engineering

Submitted by

Dost Rahman
25-FET/MS CE/F22

Supervised by

Dr. Muhammad Noman
Assistant Professor

Department of Civil Engineering
Faculty of Engineering & Technology
International Islamic University, Islamabad
November 2025

FINAL APPROVAL

It is certificate that we have read the thesis submitted by Dost Rahman and it is our judgment that this thesis is of sufficient standard to warrant its acceptance by the International Islamic University, Islamabad for the MS Degree in Civil Engineering

COMMITTEE

External Examiner ______________________

Internal Examiner ______________________

Supervisor ______________________

Chairman ______________________

DECLARATION

I hereby declare that the work presented in this thesis, entitled *Investigation of Inorganic Self-healing of Municipal Waste Concrete with Steel Fibers exposed to Elevated Temperature*, is my own original work carried out under the supervision of *Dr. Muhammad Noman (Assistant Professor)*. To the best of my knowledge, this work has not been previously submitted, either in whole or in part, for any degree or diploma at any university or institution.

I further declare that all sources of information and data used in this thesis have been duly acknowledged and referenced in accordance with academic ethics and integrity.

Engr. Dost Rahman
Registration No.:25-FET/MS CE/F22
Department of Civil Engineering
International Islamic University, Islamabad

ABSTRACT

This study evaluates a practical, construction-scale route to post-fire recovery in concrete that uses modest municipal incinerator bottom ash (MIBA) as a cement substitute, steel fibers to control crack openings, and fully inorganic healing granules. A 4 × 3 factorial matrix combined MIBA at 0%, 5%, 10%, and 15% (by cement mass) with steel fibers at 0.0%, 0.5%, and 1.0% (vol.). All mixes used w/b = 0.60 and a fixed 2% (by concrete mass) dosage of epoxy-coated inorganic granules (Na_2SiO_3/Na_2CO_3/NaOH/CaO/bentonite). One-hundred-millimetre cubes (n = 108) were tested in three states: 28-day control, after heating to 400 °C (5 $°C \cdot min^{-1}$, 2 h dwell, closed-door cooling), and after 28 days of water-based healing. Compressive strength, ultrasonic pulse velocity (UPV), and dynamic modulus (from UPV and density) quantified damage and recovery; air-cured data provided contrast where applicable.

Heating produced limited mass loss (≈1–3%) and high density retention (≈0.98–0.99 of control) with no explosive spalling. Ambient compressive strength decreased with MIBA (≈26.2 MPa at 0% to ≈19.0 MPa at 15%). Residual-to-control strength ratios fell with ash content (≈0.61 to ≈0.52 from 0%→15% MIBA). After 28-day water healing, healed-to-control ratios also declined with ash (≈0.94 to ≈0.75). Steel fibers did not materially raise ambient strength but improved residual capacity and healing efficiency; healed-to-control increased from ≈0.795 (0%) to ≈0.855 (0.5%) and ≈0.877 (1.0%). UPV collapsed after heating ($\approx 3.82 \rightarrow 2.02$ $km \cdot s^{-1}$) and recovered markedly in water (≈3.16 $km \cdot s^{-1}$; air ≈2.42 $km \cdot s^{-1}$). Dynamic modulus fell from ≈31.5 to ≈8.8 GPa and rebounded to ≈21.6 GPa with water healing (air ≈12.7 GPa).

Mechanically, recovery is meaningful but incomplete; transport and stiffness rebound further, provided moisture is available. For mixes of this type, a pragmatic specification emerges: ≤10% MIBA, 0.5–1.0% steel fibers, and guaranteed post-fire wet curing. The inorganic granules were compatible with batching at 2% mass and aided recovery without fresh-property issues. UPV-based indices are effective for triage and verification. Overall, the results support a circular, field-ready pathway to rehabilitate fire-affected concrete without relying on exotic chemistries.

Keywords: self-healing concrete; MSWI bottom ash (MIBA); steel fiber reinforced concrete (SFRC); inorganic healing granules; ultrasonic pulse velocity (UPV); dynamic modulus; residual strength; fire exposure; water curing.

TABLE OF CONTENTS

1 Contents

LIST OF FIGURES

LIST OF TABLES

1 INTRODUCTION

1.1 Background of the study

Concrete is often praised for its inherent fire resistance; nonetheless, even “survivable” thermal excursions leave a distinct fingerprint on the material: dehydration of portlandite and C–S–H, thermal incompatibility between paste and aggregates, and pervasive microcracking that diminishes stiffness and connectivity long before gross strength is lost. In the range of 200–600 °C—typical of many building fires—hydration products decompose, pore pressures rise, and the propagation of microcracks accelerates; above roughly 400 °C, residual performance deteriorates rapidly (Noman et al. 2024), with stiffness metrics generally more sensitive than compressive strength (Kodur 2014; Usman et al. 2021). While high-strength concretes are particularly prone to explosive spalling under rapid heating, conventional mixes also suffer significant transport-property damage that complicates post-event serviceability and durability (Ma et al. 2015).

Traditional repair strategies—surface overlays, crack injections, and patching mortars—can be effective but are intrusive, labor- and carbon-intensive, and difficult to deploy at scale on lightly damaged yet extensive surfaces. This has motivated sustained interest in self-healing cementitious systems that can autonomously restore continuity at the crack scale. Two broad families exist: (i) autogenous healing, which leverages unhydrated clinker and carbonation to seal fine cracks under the presence of moisture, and (ii) autonomous healing, which introduces dedicated agents (e.g., mineral, polymeric, bacterial) to trigger precipitation and binding within cracks (De Belie et al. 2018; Van Tittelboom and De Belie 2013). Autogenous healing is robust and zero-maintenance but largely confined to very small cracks and requires persistent moisture. Autonomous strategies expand the crack-width envelope and predictability, though their field robustness varies with the chemistry and delivery method (De Belie et al. 2018; Van Tittelboom and De Belie 2013).

Within the autonomous class, fully inorganic healing agents (e.g., sodium-silicate-based systems, carbonates, and alkaline earth oxides) are attractive for fire-exposed structures because their functionality is not dependent on organic carriers that can degrade with temperature. Inorganic agents can precipitate C–S–H-like gels or carbonates upon contact with pore solutions, provided adequate moisture is available. Compared with polymeric microcapsules, mineral granules offer high thermal stability, compatibility with cement chemistry, and the possibility of dosing at concrete scale using standard batching equipment (De Belie et al. 2018; Van Tittelboom and De Belie 2013). The trade-offs include ensuring uniform dispersion, avoiding segregation at practical dosages, and verifying that the agents do not unduly compromise fresh properties or baseline strength.

A complementary lever is crack-width control. Steel fiber reinforcement is well established for improving post-cracking ductility and controlling crack openings. Under elevated temperatures, steel fibers can mitigate thermal damage indirectly by bridging microcracks and maintaining load transfer after paste degradation. Reviews consistently report that steel-fiber-reinforced concrete (SFRC) exhibits better retention of tensile/flexural capacity and fracture energy after heating compared with plain concrete, and—depending on dosage and fiber geometry—a measurable improvement in residual compressive strength (L. Li et al. 2020). The underlying mechanism is not that fibers prevent dehydration or chemical damage; rather, they manage the crack process, enabling subsequent moisture-driven healing to be more effective.

For triage and verification, ultrasonic pulse velocity (UPV) is an operationally attractive, non-destructive indicator. UPV degrades sharply with thermal microcracking and dehydration, and correlates with both residual modulus and strength after heating. Numerous studies have quantified these relationships and developed prediction models linking UPV to residual mechanical properties in both normal- and lightweight-aggregate concretes across temperature bands including 400 °C. In practice, establishing an as-built UPV baseline allows post-event damage indices and healing indices to be computed, informing whether passive healing (e.g., wet curing) suffices or whether active repair is warranted.

In parallel with performance-driven repair, the cement and concrete sector is pressed to cut clinker content and valorize wastes in a circular-economy framework. Municipal solid waste incineration bottom ash (MSWI-BA or MIBA) has been widely studied as an aggregate and, to a lesser extent, as a partial binder replacement. As a binder substitute, MIBA typically exhibits lower reactivity and a lower CaO/SiO_2 ratio than Portland cement, which can depress early strength and portlandite formation unless mitigated by processing or synergy with other SCMs (Chen et al. 2023). Variability, residual metallic aluminum (which can cause hydrogen evolution), chloride/sulfate contents, and porous particle morphology are recurring concerns; washing, aging, accelerated carbonation, and milling are commonly recommended to stabilize chemistry and improve grading and packing (Chen et al. 2025; Węgliński and Martysz 2024). The technical potential is clear, but the workable replacement window without targeted pre-treatment is often limited to modest percentages if structural performance and durability are priorities.

Bringing these threads together highlights a practical opportunity: combine modest MIBA substitution for circularity, steel fibers for crack management, and fully inorganic healing granules to exploit moisture-driven precipitation, then verify recovery using UPV-based diagnostics. Thermal exposure at or around 400 °C is a particularly relevant proving ground: it is severe enough to expose weaknesses in the matrix and the healing concept, yet common enough in real buildings that demolition is not inevitable (Noman and Yaqub 2021; Yaqub 2010). The central question is not whether any one lever works in isolation, but whether a construction-ready system, fiber-controlled cracking plus inorganic healing agents, implemented at concrete scale, can deliver meaningful, measurable recovery after moderate thermal damage while accommodating limited MIBA contents.

1.2 Problem Statement

On the basis of the detailed literature review provided in chapter 2, the following problem statement has been identified for this study:

Despite growing interest in self-healing concrete, three practical questions remain unresolved for structural-scale use: (i) the extent to which moderate temperature exposure (here, 400 °C) degrades strength and stiffness when MIBA is used as a cement replacement; (ii) whether steel fibers—without changing the matrix chemistry—can enhance residual performance and healing efficiency; and (iii) whether a fully inorganic, epoxy-coated healing granule can be produced, batched, and dispersed at concrete scale without compromising fresh or hardened behavior. The industry lacks clear guidance on workable MIBA replacement levels, post-fire recovery potential, and simple diagnostic tools to decide between passive healing and active repair. This thesis addresses these gaps in a controlled, factorial study.

1.3 Objectives

To address the problem statement mentioned, the following objectives are set:

1. Quantify the effects of MIBA replacement (0%, 5%, 10%, 15%) and steel fiber content (0.0%, 0.5%, 1.0% vol.) on (a) as-cast strength and (b) residual strength and stiffness after exposure to 400 °C.

2. Assess healing efficiency under 28-day water-based curing using compressive strength recovery, UPV, and dynamic modulus; contrast results with air curing when applicable.
3. Establish UPV-based indices (damage and healing) as practical diagnostics to triage post-fire condition and verify recovery.
4. Evaluate the batching practicality of fully inorganic, epoxy-coated healing granules at 2% mass dosage in ready-mix-style production.

1.4 Scope & Limitations

The experimental program employed a fixed water-to-binder ratio (w/b = 0.60), MIBA replacement at four levels (0–15% by cement mass), steel fibers at three levels (0–1.0% vol.) using a single hooked-end geometry, and a constant healing-granule dosage (2% by concrete mass). Performance was evaluated on 100 mm cubes in three states: as-cast control, post-heating (400 °C), and post-healing after 28-day water immersion. Primary indicators were compressive strength, UPV, and dynamic modulus (from UPV and density).

Findings are bounded by: a single w/b ratio; one fiber geometry and length; a single thermal exposure level (400 °C) and heating protocol; specimen-scale testing (cubes); a fixed granule dosage; and emphasis on compressive behavior and wave-based diagnostics rather than a full mechanical/durability portfolio. MIBA in this study was sieved and cleaned but not otherwise upgraded (e.g., carbonation, milling). Field moisture gradients, wet–dry cycles, and member-scale restraint effects were not simulated.

1.5 Brief Overview of the Thesis

- **Chapter 1** introduces the problem context, states the research gap, and sets out the objectives, novelty, and scope.

- **Chapter 2** reviews the relevant literature on MIBA as a cement replacement, steel fiber reinforcement in thermo-mechanical contexts, and engineered self-healing mechanisms, with emphasis on inorganic healing systems and UPV-based diagnostics.
- **Chapter 3** details materials, mix design, healing-granule formulation and coating, specimen preparation, thermal exposure protocol, curing/healing regimes, and test methods for strength, UPV, and dynamic modulus.
- **Chapter 4** presents and discusses the experimental results, including the effects of MIBA and fiber content on control, heated, and healed states; healing efficiencies; and diagnostic indices, supported by statistical comparisons where appropriate.
- **Chapter 5** synthesizes the conclusions, draws practice-oriented recommendations, and outlines limitations and priorities for future work.

2 LITERATURE REVIEW

2.1 Cement Decarbonization

2.1.1 Why cement decarbonization matters

Cement underpins modern infrastructure but is responsible for a sizeable share of global CO_2. Unlike many sectors where emissions are mostly energy-related, a majority of cement's footprint comes from the chemistry of clinker production itself: when limestone ($CaCO_3$) is calcined to make lime (CaO), CO_2 is released (refer Eq. 2.1). Recent industry syntheses and roadmaps consistently place process emissions at roughly 60% of the sector's total, with most of the remainder from kiln fuels and a smaller slice from electricity and transport (GCCA 2024). This split is crucial because it means switching to renewable electricity alone cannot eliminate emissions; the process component must be tackled directly (Griffiths et al. 2023).

$$CaCO_3 \rightarrow \ CaO + CO_2 \qquad \text{Equation 2-1}$$

2.1.2 Emission profile and mitigation levers

Three broad sources dominate: (i) process emissions from limestone calcination; (ii) fuel combustion in high-temperature kilns (1,450 °C); and (iii) electricity for grinding and material handling. The IPCC's industry assessment (Ruane 2024) emphasizes that, because process CO_2 arises intrinsically from calcination, deep decarbonization requires measures beyond clean energy, especially clinker reduction, alternative binders, and carbon capture.

Most decarbonization roadmaps converge on a portfolio:

i. Reduce clinker per tonne of cement and per m^3 of concrete (material efficiency + SCMs),
ii. Improve thermal/electrical efficiency,

iii. Switch kiln fuels to low-carbon/biogenic alternatives, and

iv. Capture and permanently store (or utilize) remaining process CO_2 at scale. The IEA frames this as simultaneous “supply-side” shifts (production of near-zero cement) and “demand-side” shifts (efficient use/specification changes), with a 2030 milestone that near-zero options are established in all regions (Bataille 2020).

2.1.3 Clinker reduction: SCMs, LC^3, and standards

Lowering the clinker-to-cement ratio (CKR) is the fastest, lowest-cost wedge where suitable supplementary cementitious materials (SCMs) are available. In Europe, progress has been mixed: alternative fuels have advanced quickly, yet CKR has plateaued in recent years, signaling the need for new SCM streams and specification reforms that permit higher substitution without compromising performance (CEMBUREAU 2024).

Limestone-calcined clay cements (LC^3) pair abundant clays (calcined to metakaolin) with fine limestone to unlock high substitution levels (40–50% clinker replacement), while maintaining strength and durability through the synergistic carbo-aluminate chemistry. Foundational reviews (Scrivener and co-authors; later updates) report robust mechanical performance, favorable durability in many exposures, and wide geographic scalability due to clay abundance. Ongoing meta-analyses and reviews reaffirm LC^3’s potential to materially cut embodied CO_2 where slag/fly ash are scarce or costly (Scrivener et al. 2018; Sharma et al. 2021).

Unlocking clinker reduction also depends on how we use cement. The IPCC notes that performance-based standards (moving away from prescriptive high-clinker types) and green public procurement can accelerate adoption of blended and LC^3 cements without loss of safety or durability (Bataille 2020).

2.1.4 Energy efficiency and alternative fuels

State-of-the-art dry-process kilns with preheaters/precalciners, high-efficiency separators, and modern grinding (e.g., vertical roller mills) continue to push specific energy use down. While the absolute savings per tonne are incremental, they compound across billions of tonnes annually.

Shifting from fossil coke/coal to waste-derived and biogenic fuels reduces combustion emissions and can support circularity. Europe now replaces a substantial share of kiln fossil fuels with AFs (the latest industry reports cite replacement rates above 50% in the EU28), though availability, permitting, and emission controls (NO_x, SO_x, metals) remain boundary conditions (CEMBUREAU 2024).

2.1.5 Carbon capture, utilization and storage (CCUS)

Because process emissions remain even with perfect efficiency and 100% clean electricity, CCUS appears in all 2050 net-zero pathways for cement. The IPCC highlights multiple capture routes—post-combustion amines, oxy-fuel, calcium looping, and process-integrated concepts like LEILAC—plus the need for transport and permanent storage (or qualified utilization) (Bataille 2020).

From pilots to first-of-a-kind plants. In 2025, Heidelberg Materials inaugurated the world's first industrial-scale carbon capture, and storage (CCS) on a cement kiln at Brevik, Norway—designed to capture 400,000 tCO_2/yr and ship the CO_2 to the Northern Lights offshore storage site (part of Norway's Longship program). Early output ("evoZero") was reportedly pre-sold despite price premia, signaling emerging demand pull where policies and buyers align. These milestones move CCUS from concept to bankable reality, though scale-up will still hinge on storage access, carbon pricing, and offtake agreements (Beumelburg 2025).

Northern Lights started injecting CO_2 in 2025, demonstrating end-to-end capture-transport-storage with Brevik among the initial sources evidence that shared infrastructure can de-risk and aggregate volumes from multiple industrial sites.

2.1.6 Demand-side and circularity: using less, using smarter

Decarbonization is not only a kiln problem. Material-efficiency strategies, optimizing structural design, right-sizing strength classes, maximizing SCM/concrete performance, and designing for longevity—reduce the demand for high-clinker cement. The GCCA's and IEA's roadmaps both emphasize collaboration across the value chain (designers, contractors, and clients) so that mix designs and specifications reward low-carbon concretes rather than defaulting to conservative, clinker-heavy choices (GCCA 2024).

2.1.7 Roadmaps, milestones, and current progress

The Global Cement and Concrete Association (GCCA) Roadmap to Net-Zero Concrete (2050) sets actions across five pillars: reducing clinker, accelerating AF/renewables, efficiency, CCUS, and value-chain collaboration. Annual progress reports track metrics such as clinker ratio, thermal substitution rate, and the pipeline of CCUS projects (GCCA 2024).

What "near-zero" means by 2030. The IEA's Breakthrough Agenda frames a 2030 goal where near-zero cement is "established and growing in every region," which practically means early commercial CCUS units, broader acceptance of LC^3/SCM-rich blends, and procurement policies that normalize low-carbon concrete in public works (IEA 2018).

This thesis examines inorganic self-healing strategies and waste-derived constituents in concrete exposed to elevated temperature. From a decarbonization lens, such approaches contribute on two fronts: (i) enabling robust performance with lower-clinker binders (by improving crack control, healing, and service life), and (ii) valorizing suitable waste streams as partial binders/aggregates where standards allow—thereby reducing clinker demand and embodied emissions. These align with roadmap pillars on clinker reduction, circularity, and durability-led material efficiency.

2.2 Municipal Incineration Bottom Ash (MIBA)

Municipal solid waste incineration bottom ash (MIBA) is the mineral residue that remains on the grate after combustion, typically 15–25% of the original waste mass, and contains a heterogeneous mix of glassy silicates, unburnt minerals, metals (and metal alloys), and salts. Compared with natural sand or gravel, MIBA particles are lighter, more porous, and rougher; chemically they carry chlorides and sulfates and, critically, residual metallic Al/Zn that can react in alkaline pore solution. These features make MIBA both promising (for circularity and clinker/aggregate substitution) and challenging (for durability, gas evolution, and leaching control) in cementitious systems (Chen et al. 2023).

2.2.1 Generation, composition, and environmental considerations

Fresh MIBA typically has high pH (11–12), variable moisture, and contains trace heavy metals (Cu, Pb, Zn, etc.) and organic residues. Leaching behavior improves markedly after natural "aging"/weathering and especially after accelerated carbonation, which lowers pH and immobilizes many cations; however, some anions (e.g., Sb, Cr) can remain problematic and must be checked against local limits. Several studies show that 1–3 months of aging and/or accelerated carbonation substantially reduce heavy-metal release, with depth of carbonation and fraction size governing the effect (Arickx, Van Gerven, and Vandecasteele 2006; Wehrung et al. 2024).

A well-documented risk specific to MIBA is the presence of metallic aluminum: in highly alkaline pore solution, Al reacts with water to produce hydrogen gas, causing expansion, voids, and early cracking if ash is used without appropriate pre-treatment. Quantitatively, 1 g of Al can evolve almost 1.24 L of H_2 at STP, most vigorously within the first 50–150 minutes after mixing, so stabilizing or removing reactive Al is a prerequisite for structural applications (Malaiškienė, Spudulis, and Stonys 2023).

2.2.2 Pre-treatment and upgrading routes

Four families of treatments dominate the literature: (i) aging/weathering (natural storage to carbonate and hydrate reactive phases), (ii) washing (to remove salts and fines), (iii) carbonation (natural or accelerated CO_2 treatment), and (iv) mechanical or thermal conditioning (screening, metal separation, wet-grinding/milling, heat treatment). Aging for ≥3 months lowers pH and improves leaching; washing reduces chlorides and improves consistency; carbonation immobilizes many metals and mitigates Al activity; and milling/wet grinding densifies particles and helps avoid hydrogen-related swelling. Advanced metals recovery (magnetic + eddy-current + optical sorting) further removes residual metals and raises product quality for concrete (Kumpueng, Phutthimethakul, and Supakata 2024; Phutthimethakul and Supakata 2022; Zhang and Zhao 2014).

2.2.3 Roles in cementitious materials

Pre-washed / graded MIBA can partially replace fine or coarse aggregates. A consistent trend is reduced density and, at high contents, lower strength due to higher porosity and water absorption; careful pre-treatment and modest replacement levels (often ≤30% of fine or ≤50% of coarse by volume, depending on grading and treatment) preserve acceptable performance. Durability indicators such as sorptivity and permeability can worsen if the ash is untreated, so mix design often pairs MIBA with low w/b, SCMs, or surface densification to offset transport (Kumpueng, Phutthimethakul, and Supakata 2024; Zhang and Zhao 2014).

As cement/SCM replacement or microfiller. Early work showed MIBA's potential as a mineral addition, but chloride content and low intrinsic reactivity limit direct cement replacement without processing. Recent studies evaluate milled MIBA as a microfiller / low-level SCM: milling increases fineness and glass exposure, but Al-driven expansion remains a risk if metallic phases are not neutralized; net effects include slower hydration heat and modest strength penalties at higher dosages. In practice, low replacement levels after thorough treatment (and compliance with chloride limits) are recommended (Chen et al. 2023, 2025; Pera et al. 1997).

When used in alkaline activation, MIBA can participate in forming binding gels, but metallic Al is again detrimental to strength and dimensional stability unless removed or passivated. Reviews emphasize coupling pre-treatment (e.g., metal removal, carbonation) with tailored activation to achieve stable AAM performance (Chen et al. 2025).

2.2.4 Mechanical and durability performance in concrete

Across many campaigns, untreated MIBA tends to reduce compressive strength and modulus as replacement level rises, primarily due to higher porosity/absorption and weaker interfacial transition zones. Pre-washing and optimized grading can narrow the gap, and some industrial trials report strength recovery at low additions where internal pores are effectively filled; nevertheless, a conservative ceiling on replacement is common in structural concrete. Durability-wise, higher water uptake and sorptivity are frequently reported; carbonation depth may increase with MIBA because of higher permeability, while chloride and sulfate resistance depend strongly on ash salt content and matrix quality. These findings support the need for (i) mandatory salt removal/limits, (ii) low w/b and SCM synergy, and (iii) verification testing under project-specific exposures (Bakker et al. 2025; Zhang and Zhao 2014).

2.2.5 Knowledge gaps relevant to this thesis

Despite rapid progress, several gaps remain pertinent to performance-based, low-carbon concretes:

a. long-term chloride/carbonation coupling in MIBA concretes under marine/urban exposures;
b. standardized pass/fail criteria for hydrogen-related expansion in cementitious matrices;
c. microstructure-level evidence linking specific pre-treatments (e.g., semi-dry carbonation + wet grinding) to ITZ densification and transport reduction; and
d. behavior after thermal excursions (e.g., fire)—including whether MIBA's porosity/internal curing capacity alters post-fire cracking and healing.

Addressing these gaps would help translate circular-economy benefits into robust, codified structural use.

2.3 Self-healing of Concrete

2.3.1 Concepts and mechanisms

Concrete can restore part of its performance after cracking by processes that occur without external intervention ("autogenous" healing) and by deliberately embedded systems that are activated by damage ("autonomous" or "autonomic" healing). RILEM TC 221-SHC consolidated the terminology and early protocols, distinguishing self-sealing (transport recovery) from mechanical self-healing, and emphasized controlled pre-cracking, exposure, and recovery indices for comparability (Mario de Rooij; Kim Van Tittelboom; Nele De Belie; Erik Schlangen 2013).

Autogenous healing is driven primarily by continued hydration of unhydrated clinker and by precipitation of $CaCO_3$/C-S-H in the presence of water; it is strongly environment-dependent and most effective for small crack widths. Seminal reviews and subsequent studies report reliable sealing at sub-millimetric scales (often ≤ 0.1 – 0.2 mm), with wider ranges possible depending on mix design, age, and curing regime (De Belie et al. 2018; Van Tittelboom and De Belie 2013).

2.3.2 Autogenous healing: governing parameters and expected range

Water supply is the dominant trigger. Under water immersion or wet–dry cycles, concrete exhibits faster and more complete sealing than under sealed humidity; early-age materials, with higher clinker reactivity, heal more readily. Transport recovery (e.g., water permeability reduction) typically exceeds strength recovery because mineral infill can seal flow paths without fully restoring fracture bridging. Representative testing shows complete closure for ≲0.15 mm and significant closure up to 0.35–0.40 mm under water exposure; humidity-only curing yields limited effects (Roig-Flores and Serna 2020).

Quantification follows RILEM-aligned procedures: (i) optical crack-closure ratios; (ii) permeability-based healing indices comparing post-healing to the cracked state; and (iii) mechanical recovery via reloading in bending/tension with controlled crack opening. Recent work highlights the need to report both transport and mechanical indices to avoid over-interpreting visual closure (Lee et al. 2021).

2.3.3 Autonomous systems with emphasis on inorganic agents

Because autogenous healing is limited by moisture and crack size distribution, autonomous systems have been developed to extend the effective range and repeatability. Among these, inorganic/mineral agents are attractive for compatibility, durability, and thermal robustness relative to many polymers.

2.3.3.1 Sodium-silicate systems

Liquid sodium-silicate (SS) encapsulation is well established: capsules fracture upon cracking, releasing SS that reacts in the alkaline pore solution to form sealing hydrates/gels, reducing permeability and sometimes improving stiffness recovery. Polyurethane/urea-formaldehyde or polyurea shells are common; optimization studies demonstrate stable capsules and effective transport sealing in mortar/concrete. High-temperature analogs in oil-well cements (80 °C) confirm functionality under elevated service temperatures (Beglarigale et al. 2018; Qureshi, Kanellopoulos, and Al-Tabbaa 2016).

A complementary route uses cementitious or lightweight-aggregate carriers impregnated with SS, enabling larger payloads and good dispersion at concrete scale; improvements in post-cracking modulus and permeability have been reported at practical dosages.

2.3.3.2 MgO / CaO / bentonite (expansive mineral) capsules and pellets

Encapsulated expansive minerals (reactive MgO, quicklime/CaO, bentonite) hydrate/carbonate after water ingress, generating solid products and slight expansion that fill and bridge cracks. Concentric glass macrocapsules (mineral + water) demonstrated robust crack sealing under ambient, high-humidity, and immersion regimes; more recent granulation/encapsulation approaches yield fully inorganic capsules with improved handling. Reviews highlight reactive MgO combined with clays as a durable, compatible system for autonomous sealing (J. Li, Guan, and Zhang 2023; Lima et al. 2024; Qureshi, Kanellopoulos, and Al-Tabbaa 2016).

2.3.3.3 Carbonate and related chemical stimulators

Alkali carbonates (e.g., Na_2CO_3) can accelerate $CaCO_3$ precipitation and stimulate early sealing; effectiveness and mechanical trade-offs depend on binder chemistry and dosage. A recent review of chemical-based self-healing summarizes these pathways and encapsulation options relevant to mineral systems (Adhikary et al. 2024).

Other autonomous strategies include polymeric capsules, vascular (micro-vascular) networks, and microbially induced $CaCO_3$ precipitation (MICP). These have produced strong sealing under wet regimes and notable demonstrators, but thermal survivability and long-term nutrient management can constrain post-fire applications. Hence the motivation for inorganic systems in this thesis.

2.4 Use of Steel Fibers for Self-healing

2.4.1 Rationale and primary mechanisms

Steel fibers are widely adopted to mitigate crack localization and to keep service-level cracks tight and numerous rather than few and wide. This crack-width control is the key "enabler" of self-healing: narrow, tortuous cracks favor precipitation of healing products (e.g., $CaCO_3$, C-S-H) and shorten transport paths, so flow drops sharply even when mechanical properties only partially recover. Contemporary reviews of fiber-reinforced cementitious composites (FRC) consistently report superior self-sealing in steel-fiber-reinforced concrete (SFRC) versus plain concrete under wet or wet–dry exposures, precisely because fibers limit residual crack openings and stabilize multiple micro-cracks (Amran et al. 2022).

Beyond width control, steel fibers alter crack surface topology and roughness, especially under cyclic or freeze–thaw damage, thereby enhancing interlock and providing additional nucleation sites for mineral infill; permeability reductions are then observed for a given nominal crack width. Experimental studies quantifying flow through cracked SFRC show reduced water/gas permeability and slower permeability evolution versus unreinforced matrices.

2.4.2 Synergy with healing promoters (crystalline/mineral routes)

Because fibers keep cracks within the “healable” window, coupling SFRC with crystalline admixtures or other mineral promoters often yields additive benefits. In SFRC and HPFRC, crystalline admixtures have been shown to accelerate sealing of cracks under immersion and saline exposures, lowering steady-state permeability and delaying chloride penetration. Protocols developed for these composites quantify multi-performance “healing-induced recovery indices” for transport and mechanical metrics (Escoffres, Desmettre, and Charron 2018; Ferrara, Krelani, and Moretti 2016).

Recent studies extend this synergy to bio-mineralization (bacteria-based $CaCO_3$ precipitation) in the presence of steel fibers: fibers bridge and limit crack width while the biological agent supplies carbonate; together they enhance sealing and durability indicators relative to either approach alone (Helal et al. 2024).

2.4.3 Quantitative effects and governing parameters

The magnitude of steel-fiber benefits depends on: (i) volume fraction and geometry (e.g., hooked-end, aspect ratio), which control bridging stresses and residual crack openings; (ii) fiber orientation/dispersion, affecting the probability of effective bridging across a given crack; and (iii) loading history and exposure, which dictate whether healing products can precipitate and remain stable. Across multiple campaigns, increasing steel-fiber content reduces post-cracking flow at a given crack opening and slows degradation of water resistance under sustained load or cycles.

A practical implication for design and testing is that reporting initial and residual crack widths, not merely maximum load or toughness, is essential when comparing “healing efficacy” in mixes with different steel-fiber dosages or geometries. Current reviews explicitly tie self-healing outcomes to crack-width distributions produced by the fiber system.

2.5 Effects of Fire on Concrete

At the material scale, heating drives dehydration of C–S–H (≈100–300 °C) and dehydroxylation of portlandite (400–600 °C), coarsening the pore system and reducing stiffness/strength; differential thermal expansion between aggregates and paste adds microcracking, with high-silica and dense, low-permeability mixes often more prone to explosive spalling during fast heating. Classic syntheses and NIST reports further show that spalling risk correlates with hygro-thermal pore-pressure buildup and rapid temperature rise; mitigation by polypropylene micro-fibres (≈1–2 kg/m^3) is widely evidenced because melting around 170 °C creates transient venting channels that relieve vapour pressure. Design-level consequences are captured in fire design provisions—EN 1992-1-2 and ACI 216.1/TMS 216—which give temperature-dependent material reduction factors and calculation/ tabulated methods consistent with standard fire exposures (e.g., ISO 834/ASTM E119). Current RILEM TC 256-SPF recommendations also standardize how to screen and quantify spalling propensity (specimens, storage, boundary conditions, heating), supporting reproducible laboratory assessment (Khoury 2008; Kodur 2014; Krzemień and Hager 2015; Noman et al. 2024).

2.6 Post-Fire Repair of Concrete

Post-fire intervention starts with structured diagnosis: detailed mapping of colour change, cracking and spalls; targeted NDT (e.g., rebound, UPV, IR thermography) to localize delaminations/voids; and confirmatory coring with petrography (ASTM C856) to read microcracking and temperature markers, complemented where needed by XRD/TGA for phase changes. Widely used guides (Concrete Society TR 68; fib Bulletin 46) emphasize combining these methods to classify damage depth/severity before selecting repair. Compatible options include removal and recasting/shotcrete overlays, section enlargement or RC jacketing, injection (EN 1504-5), and externally bonded FRP or steel plate systems; selection is governed by verified residual capacity, durability demands, and future fire strategy (e.g., fire protection for FRP adhesives). Acceptance and quality assurance are aligned to ACI 562 for evaluation/repair design (with EN 1504 Parts 2/4/5/9/10 for products and site execution), and—where appropriate—by proof load testing to ACI 437.2 to verify post-repair performance in situ. Case syntheses report that when peak temperatures were moderate and damaged cover is fully replaced, substantial recovery of stiffness, strength and watertightness is achievable; severe section loss or high-temperature exposure may necessitate partial replacement or demolition with monitoring of the rebuilt works (Noman, Yaqub, Abid, et al. 2022; Noman, Yaqub, Fahad, et al. 2022; Usman et al. 2021; Yaqub, Bailey, and Nedwell 2011).

2.7 Concluding remarks and identified research gaps

The literature establishes that cementitious materials possess meaningful autogenous self-sealing capacity when crack widths are very small and sustained moisture is available; autonomous systems can broaden this window, and steel fibers are a practical enabler by stabilizing tight, distributed cracks. However, when this knowledge is mapped onto realistic exposure scenarios; especially thermal excursions and post-fire rehabilitation, several consistent gaps emerge. The following synthesis distills the gaps that motivate the experimental program of this thesis.

1. Reporting is still inconsistent across studies: initial/residual crack widths, crack-width distributions (not just maxima), healing exposure histories (immersion vs wet–dry vs RH), and the simultaneous use of both transport and mechanical recovery indices are often incomplete. Visual “closure” is regularly overinterpreted, while flow/permeability and stiffness/strength recoveries are not reported together. There is also limited adoption of

standardized pre-cracking and reloading methods for fiber-reinforced mixes, and scarce round-robin style validations for permeability-based healing indices.

2. Many campaigns demonstrate short-term self-sealing, yet the long-term stability of mineral infill (C-S-H/$CaCO_3$) under service aggressors (chlorides, carbonation, sulfates, freeze–thaw, sustained or cyclic loads) remains under-quantified. The persistence of transport recovery under repeated damage–healing cycles is likewise insufficiently documented.
3. Autonomous mineral systems at structural scale. Inorganic agents (e.g., sodium silicate, MgO/CaO/bentonite, carbonate stimulators) are promising for durability and thermal robustness, but most evidence is on mortar specimens or small prisms. There are few concrete-scale studies that jointly optimize payload, delivery (capsules/granules/impregnated carriers), workability, and mechanical trade-offs; reliability and repeatability under field-relevant dispersions/orientations also require clarification. Mechanical recovery (beyond watertightness) remains modest and poorly predicted.
4. While steel fibers clearly aid healing by controlling crack widths, quantitative design rules linking fiber content/geometry/orientation to service-level crack-width distributions—and hence to expected healing indices—are not established. Interactions with crystalline admixtures and mineral capsules are encouraging but reported with heterogeneous protocols. The effects of fiber corrosion on long-term healing performance, bond, and re-healing capacity are insufficiently resolved.
5. The interface between self-healing and thermal damage remains a major gap. After heating (e.g., 200–600 °C), there is limited evidence on (i) survivability and triggerability of inorganic healing agents, (ii) kinetics of re-hydration and precipitation during post-fire re-

curing, (iii) the extent to which transport and mechanical properties can be recovered in steel-fiber concretes, and (iv) durability of the healed microstructure under subsequent chloride ingress or cyclic environmental loading. Biological routes have additional survivability constraints, underscoring the need to evaluate inorganic systems post-fire.

6. Most healing studies are performed on unloaded or short-term-loaded coupons. Structural members experience restraint, sustained service load, and multi-axial stress states that influence crack opening and healing product retention. Member-scale investigations (beams/slabs/walls) that track healing under sustained or cyclic loading and realistic restraint are still rare.
7. Integration with repair practice. Current post-fire repair guidance emphasizes condition assessment and conventional repair/strengthening. There is little procedural guidance on when and how to use self-healing (autogenous stimulation or autonomous mineral agents) as part of post-fire rehabilitation (e.g., within overlays, grouts, or injected systems), how to verify performance in situ, or how to incorporate healing-driven transport recovery into acceptance criteria or life-cycle design.
8. Predictive models that couple crack-width statistics, moisture/ion transport, agent release/chemistry, and precipitation kinetics into reliability-based performance predictions are limited. There is a need for validated models that can inform design decisions (e.g., required fiber content and healing-agent dosage to meet permeability targets at given service exposures).
9. Life-cycle and techno-economic assessments comparing self-healing strategies with conventional repair/maintenance—particularly for post-fire scenarios—are scarce.

Practical guidance on cost-optimal dosages, expected maintenance deferral, and end-of-life implications is not yet available.

Responding to these gaps, this thesis concentrates on inorganic, multi-component healing granules combined with steel fibers, tested at concrete scale under controlled crack widths, moderate heating, and post-fire re-curing. The program adopts dual performance metrics (transport and mechanical recovery), documents crack-width statistics and exposure history, and includes microstructural/chemical evidence of healing. By doing so, it aims to (i) quantify the post-fire healing potential of mineral systems in steel-fiber concretes, (ii) establish design-relevant links between fiber parameters, crack control, and recovery indices, and (iii) provide actionable guidance for incorporating self-healing into post-fire repair strategies.

3 EXPERIMENTAL PROGRAM

3.1 Materials

Ordinary Portland cement (OPC) was used in a nominal proportion of 1:1.5:3 (cement:fine aggregate:coarse aggregate) by weight with a fixed water-to-binder ratio (w/b) of 0.60. Locally available crushed limestone aggregates were used as the primary aggregate system due to their ready availability in the region and consistent quality control. Aggregates were used in saturated-surface-dry (SSD) condition and conformed to conventional grading and cleanliness requirements (ASTM-C33/C33M-18 2018). Moisture corrections were applied prior to batching to maintain the target w/c ratio.

Municipal incinerated bottom ash (MIBA) was obtained from a local municipal solid-waste incineration plant. The ash was collected from the furnace bottom after the quench/de-ashing stage, air-dried, and screened to remove oversized particles and debris. Ferrous inclusions were removed magnetically, and any visible non-mineral contaminants were hand-picked where necessary. The ash was then oven-dried (105 °C) to constant mass and sieved to obtain a fine fraction (passing 75 µm) suitable for partial cement replacement. The retained coarse fraction was discarded. XRD (see Figure 3-1) of the MIBA shows strong crystalline reflections, dominated by quartz (26.5°) and calcite (29.5°), with weaker peaks attributable to hematite and corundum. The predominance of crystalline phases indicates low intrinsic reactivity, suggesting that additional conditioning e.g., fine grinding, washing/aging, or accelerated carbonation may be required to improve its reactivity. The XRF results showing the percentage oxides of MIBA are compared with the OPC are provided in Table 3-1. MIBA replaced cement at 0, 5, 10, and 15% by mass of cement, with the total binder mass held constant across mixes. The ash was stored in sealed containers to prevent moisture uptake prior to use. Figure 3-2 shows the finally grind, cleaned and prepared MIBA samples used in this study.

Commercial carbon-steel fibers (as shown in Figure 3-3) with hooked-end were used with the nominal dimensions of 25 mm (length), and 0.5 mm (diameter). The mechanical properties of the fibers were taken as reported by the supplier i.e., Tensile strength = 345 MPa and elastic modulus = 200 GPa. The fibers were used as received and stored dry.

An inorganic, multi-component healing agent was produced as spherical granules and later coated to improve handling and resist agglomeration during mixing. The core powder blend comprised sodium silicate, sodium carbonate, sodium hydroxide, quicklime (CaO), and bentonite clay in the mass fractions shown in Table 3-2. Dry powders were blended to homogeneity, after which distilled water was introduced slowly in a rotary granulation mixer to nucleate and round the particles. The wet granules were tray-dried in a ventilated oven for 24 h, then allowed to cool to room temperature (see Figure 3-5). A thin epoxy-resin coating was applied as a protective barrier; immediately after coating, the granules were lightly dusted with cement to suppress surface tack and reduce inter-particle adhesion. The resulting granules exhibited an average diameter of 8 mm (visual sieve check), a smooth outer shell, and sufficient handling robustness for batching (see Figure 3-5). Prior to use they were stored in sealed containers. In the concrete mixtures, the granules were dosed at 2% by mass of concrete.

Table 3-1:Comparison (% Weight) of Oxides using XRF

Oxide		**MIBA**	**OPC**
Calcium Oxide	CaO	44.54	62.01
Silicon Dioxide	SiO_2	21.86	21.01
Aluminium Oxide	Al_2O_3	7.48	5.32
Ferric Oxide	Fe_2O_3	4.47	3.19

Sulphur Trioxide	SO_3	2.55	1.55
Magnesium Oxide	MgO	2.79	2.62
Potassium Oxide	K_2O	1.63	-
Sodium Oxide	Na_2O	1.98	-
Others		0.01	-
Loss of Ignition	LOI	12.60	1.88

Table 3-2: Composition of self-healing granule

Raw Material	Sodium Silicate	Sodium Carbonate	Sodium Hydroxide	Quick Lime (CaO)	Bentonite
% Composition	40	20	10	20	10

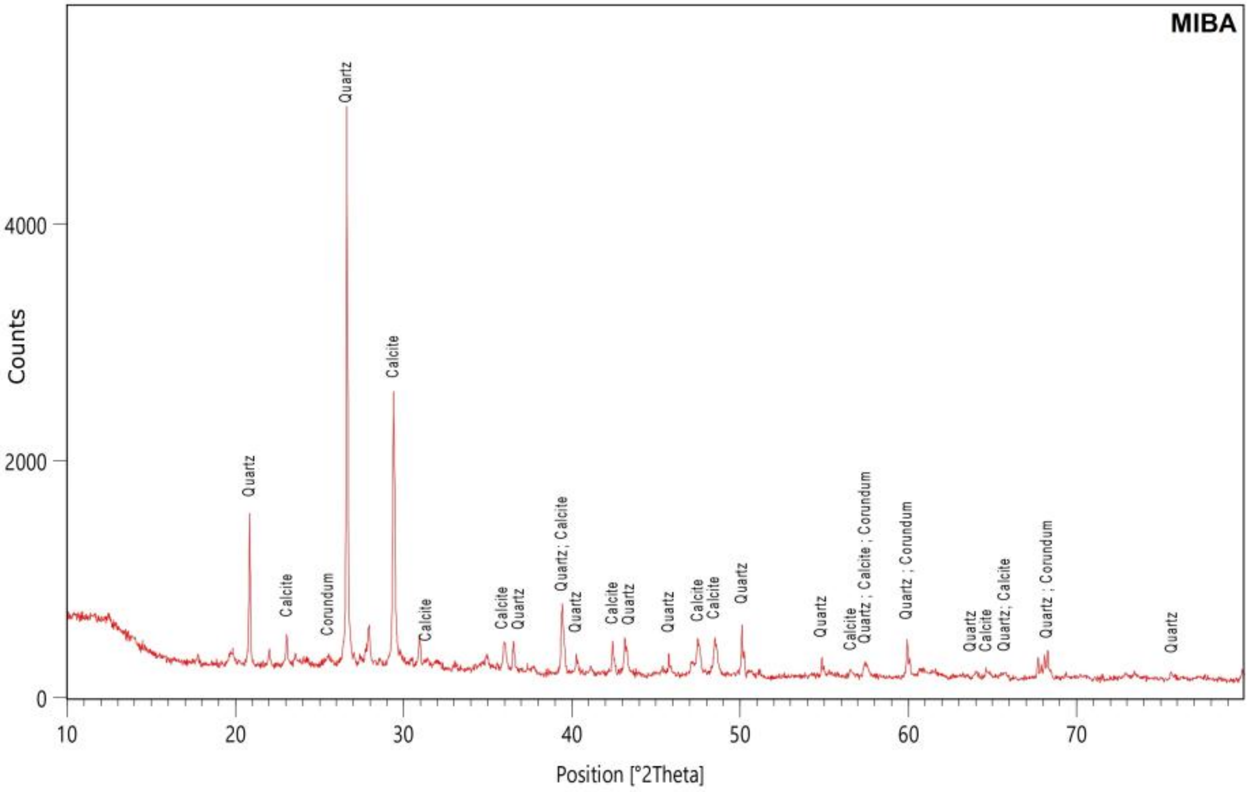

Figure 3-1: X-ray Diffraction of MIBA

Figure 3-2: MIBA collected and leaned

Figure 3-3: Steel Fibers as provided by the vendor

Figure 3-4: Preparation of Granules in a batch

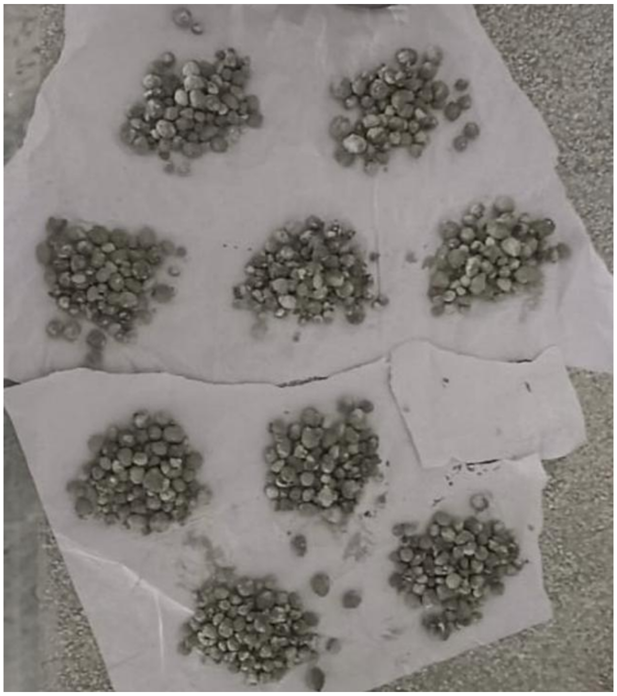

Figure 3-5: Granules for each batch of the Concrete

3.2 Specimen Preparation

All concretes were produced by mass in a laboratory pan mixer (0.15 m^3 nominal, 25 rpm) at (25 ± 2) °C. For each target combination of MIBA replacement (0, 5, 10, 15 % by mass of cement) and steel-fiber dosage (0, 0.5, 1.0%), the binder was pre-blended (OPC + MIBA) to the specified level and combined with saturated surface dry crushed limestone aggregates. Mixing followed a fixed sequence and timing to ensure repeatability. First the dry blending for 60 s of pre-blended binder and aggregates, after which water was added to achieve w/b = 0.60 followed by 120 s wet mixing. Steel Fibers were gradually added for over 60 s with a further 60 s mixing to obtain visual uniformity. Finally, the inorganic self-healing granules (average diameter = 8 mm) dosed at 2% by mass of concrete were added for 30 s. The slow addition of the epoxy-coated granules was to avoid abrasion while achieving even distribution.

Fresh properties were checked on every batch and used as acceptance criteria with slump (ASTM-C143 2015) targeted 60–90 mm, and density (ASTM-C138 2023) within ± 20 $kg \cdot m^{-3}$ of the control-mix mean. No chemical admixtures were used. Fibers were dosed as used in the experimental program and added slowly to avoid balling. Fresh concrete was placed into steel cube moulds of 100 mm internal dimension, cleaned and lightly oiled beforehand. Moulds were filled in two approximately equal lifts; each lift received 10–15 s of equivalent internal rodding to expel entrapped air. Surfaces were struck off flush and covered to limit evaporation. Demoulding occurred at 24 h, after which specimens were transferred to water curing at 20 °C until the designated reference age (28 d) prior to any further conditioning. Curing tanks were refreshed at least twice weekly. Figure 3-6 shows the samples placed in the laboratory, ready for testing.

The nomenclature of the samples is provided in the Table 3-3. As an example, M_{15}–S_{10}–F–r_3 would mean a specimen with 15 % MIBA replacement and 1% steel fiber dosage, heated to 400 °C, and the third sample of the same condition.

Figure 3-6: Samples after being cast and ready for testing

Table 3-3: Specimen nomenclature and coding scheme

Code Field	**Description**	**Allowed Values**	**Example**
M_{xx}	MIBA replacement (% of cement, rounded to 2 digits)	00, 10, 20, 30	M_{20} → 20% MIBA
S_{yy}	Steel-fiber dosage (%, expressed as used; 0.5 → 05)	00, 05, 10	S_{05} → 0.5% steel fiber
H /C/R	Conditioning state	C = Control; F = Furnace 400 °C; R = Post-heating healed	F → furnace-exposed
r_n	Replicate index	r_1, r_2, r_3	r_2 → replicate 2

3.3 Heating, Curing & Testing

Before furnace exposure, all specimens allocated to the thermal set were air-dried for 72 h at 20–25 °C and 50–60% RH to harmonize moisture content and reduce spalling risk. Thermal exposure was carried out in a programmable furnace using a 5 $°C \cdot min^{-1}$ ramp to 400 °C, 2 h peak dwell, and closed-door cooling to < 100 °C prior to handling. Figure 3-7 shows the heating setup for concrete specimen in muffle furnace. The time-temperature profile, measured using the built-in K-type thermocouple inside the furnace is provide as Figure 3-8.

Specimens in the post-heating repaired (healed) set were, after cooling, immersed in water at (20 ± 2) °C for 28 d (no external repair agents were applied). Healing duration was recorded from immersion start to the test day. Except for the specified conditioning (Control; 400 °C; Healed), production and curing procedures were identical across all mixes.

For each of the 12 mix combinations (4 × 3 factorial), three 100-mm cubes per condition (Control, 400 °C, Healed) were cast, yielding 108 cubes in total. Allocation to conditions was randomized immediately after demoulding to minimize batch effects. The above mixing sequence, timings, acceptance windows, and conditioning parameters are consistent with published practice for fiber-reinforced concretes and low-temperature fire exposures (400 °C) used to study residual and recovered performance.

Figure 3-7: Heating of concrete specimen in the Muffle furnace

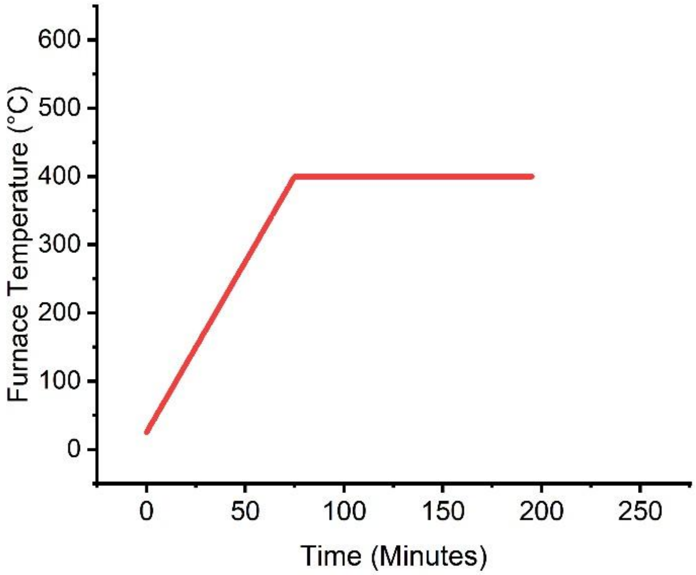

Figure 3-8: Furnace time-temperature profile

3.4 Non-Destructive Testing

This section describes the ultrasonic pulse velocity (UPV) procedure adopted for concrete cubes using a UPV apparatus from CONTROLS. UPV was used as a comparative, non-destructive indicator of internal damage (microcracking, voiding) and subsequent recovery after the post-heating healing regime.

3.4.1 Principle

A compressional (P-wave) pulse generated by the transmitting transducer travels through the specimen and is detected by the receiving transducer. The transit time t (μs) is measured electronically; the path length L (mm) is the precise distance between transducer contact faces. The pulse velocity is computed as:

$$V = \frac{L}{t}$$

Equation 3-1

V relative to a baseline indicate increased cracking/porosity; increases after the healing regime indicate microstructural recovery. Because velocity is moisture- and temperature-dependent, conditioning and ambient control were kept consistent for all readings.

3.4.2 Apparatus and accessories

i. UPV main unit from CONTROLS with paired P-wave transducers (manufacturer-supplied pair). Coaxial leads and spring-loaded transducer holders (where available) for constant contact pressure.
ii. High-viscosity ultrasonic gel (non-staining).
iii. Precision steel rule or digital caliper for path-length measurement.
iv. Clean lint-free cloths and isopropyl wipes for surface preparation.
v. Log sheet (specimen ID, age/condition, path, readings, ambient).

3.4.3 Specimen conditioning and test timing

i. All UPV measurements were performed on saturated surface-dry (SSD) cubes to minimize variability due to moisture state.

ii. For baseline readings (pre-heating), specimens were stored and tested under the same laboratory ambient used for curing.

iii. For post-heating measurements, specimens were allowed to cool to ambient (no forced quenching) and return to SSD before testing.

iv. For post-healing measurements, specimens were gently towel-dried to SSD immediately after removal from the healing medium, then tested within the same session.

v. Ambient temperature and RH were recorded for each test set; tests were run at ~constant room conditions within the lab.

3.4.4 Calibration and instrument checks (each test session)

i. Inspected leads, connectors, and transducer faces; power on the unit and verify stable battery/line power.

ii. performed the manufacturer’s zero or reference-bar check from the CONTROLS menu (auto-calibrate timebase); confirm stable repeatability (±0.2% or better).

iii. set receiver gain high enough for a clean first-arrival without clipping; set trigger/threshold to suppress noise. Keep settings constant throughout a session.

Refer to Figure 3-9 for calibration procedure of the UPV

3.4.5 Measurement procedure (per axis)

i. The transmitter and receiver were placed centrally on the two opposite faces.

ii. The measurements were displayed on the screen and recorded in the excel sheets.

iii. The transducers were lift and reseat to take three readings along the same axis, relocating a few centimeters around the face center to avoid local anomalies.

iv. The velocity was computed for three times as V=L/t. A mean of three values was recorded.

v. If any reading deviates by >3% from the axis mean or shows unstable triggering, the value was discarded and readings were again taken.

Refer to Figure 3-10 for the measurement procedure of the samples using UPV.

Figure 3-9: Calibration of the UPV

Figure 3-10: UPV testing of the specimens

4 RESULTS AND ANALYSIS

This chapter presents the experimental results and their interpretation for concrete incorporating municipal incineration bottom ash (MIBA), steel fibers, and inorganic self-healing granules subjected to a 400 °C thermal excursion and subsequent re-curing. The analyses cover fresh and hardened properties with emphasis on post-fire performance: compressive strength, ultrasonic pulse velocity (UPV)–based damage and recovery indices, and mass–density changes across conditioning states (control → heated → healed). To place the findings on a common basis, residual ratios and healing efficiencies are reported alongside narrative comparisons to established literature on self-healing and fiber-reinforced concretes. Where appropriate, derived quantities (e.g., dynamic modulus from UPV; oven-dry density from gravimetrics) are used to cross-validate trends and to offer practical metrics for post-fire assessment.

4.1 Oven-dry density and mass change under heating

To isolate the effects of temperature from moisture variability, specimens have been dried to constant mass at 105 ± 5 °C before and after thermal exposure, and oven-dry density has been computed from the measured mass and the 100 mm cube volume. Under the adopted heating regime (5 $°\mathrm{C}\cdot\mathrm{min}^{-1}$ ramp to 400 °C with a 2 h dwell and slow cooling), the oven-dry mass has decreased by 3–6 % when the comparison has been made between saturated-surface-dry (SSD) condition and the post-heating oven-dry state, and the corresponding oven-dry density has retained 0.95–0.98 of the control value. When the baseline has been taken as oven-dry at 105 °C (control) and compared with oven-dry after heating, the additional, irreversible mass loss attributable to gel-water removal from C–S–H and the onset of portlandite dehydroxylation has been 1–3 %, and the density has retained 0.98–0.99 of the control. These magnitudes have been consistent across the matrix family and have confirmed that, at 400 °C, the principal changes have been dehydration and modest microcrack-induced porosity rather than aggregate decomposition or severe solid loss. Table 4-1 shows the mass loss and the density retention ratio [ρh/ρ0] when the samples were exposed to the elevated temperature of 400 °C temperature in the muffle furnace.

The influence of mixture variables has been modest but systematic. Increasing MIBA replacement to 15 % has produced a 0.2–0.6 percentage-point increase in the total mass loss relative to the corresponding 0–10 % MIBA mixes, reflecting the slightly higher pore volume and water uptake of the ash-bearing paste. Steel fibers in the range 0.5–1.0 % by volume have not altered mass loss directly (the steel phase has remained stable in this temperature range); however, the fiber bridging has constrained crack opening, and the associated oven-dry density retentions have remained within the upper halves of the reported bands. No explosive spalling has been observed under the present heating rate and pre-drying protocol; surfaces have exhibited the light colour change and fine edge microcracking typical of paste dehydration at this temperature.

Table 4-1: Mass Loss and Density Retention (ρh) to Unheated Density (ρ0) after exposure to 400 °C

MIBA (%)	Mass loss (%)	Density retention ρh/ρ0
0	3.5	0.968
5	3.8	0.965
10	4.2	0.960
15	4.7	0.955

4.2 Effects of MIBA on Compressive Strength

Figure 4-1 shows that introducing municipal-solid-waste incineration bottom ash (MIBA) as a cement replacement produced a clear, dosage-dependent reduction in compressive strength. Averaged across fiber dosages, the control strength declined from 26.2 MPa at 0% MIBA to 24.6 MPa (5%), ≈22.7 MPa (10%), and 19.0 MPa (15%) (27% decrease over 0–15%). After heating to 400 °C, the retained capacity also fell progressively with MIBA. The 400 °C/Control ratio moved from 0.61 (0%) and 0.59 (5%) to 0.56 (10%), then 0.52 (15%). Following water recuring, recovery remained high at low MIBA and dropped more noticeably only at the upper level: Healed/Control 0.94 (0%), 0.89 (5%), 0.79 (10%), and 0.75 (15%).

It can be noted that across 0–10% MIBA, the additional penalty, both in thermal loss and in post-heating recovery, is modest. In this range, fine MIBA can act as an inert/filler and the dilution of clinker is limited, so the matrix retains much of its load-bearing capacity and remains responsive to re-hydration during water curing. Moreover, at 15% MIBA the effect becomes pronounced where, baseline strength drops more steeply, the residual capacity after 400 °C is lower, and the healing ratio diminishes. This transition is consistent with (i) clinker dilution (fewer hydration products available to carry load), (ii) higher capillary porosity and a weaker ITZ, which aggravate microcracking under heat, and (iii) reduced re-hydration potential because less unhydrated clinker remains to fuel strength recovery. In short, MIBA has only a small additional influence on strength loss and recovery up to about 10%, whereas 15% marks a clear deterioration in both residual strength and regain.

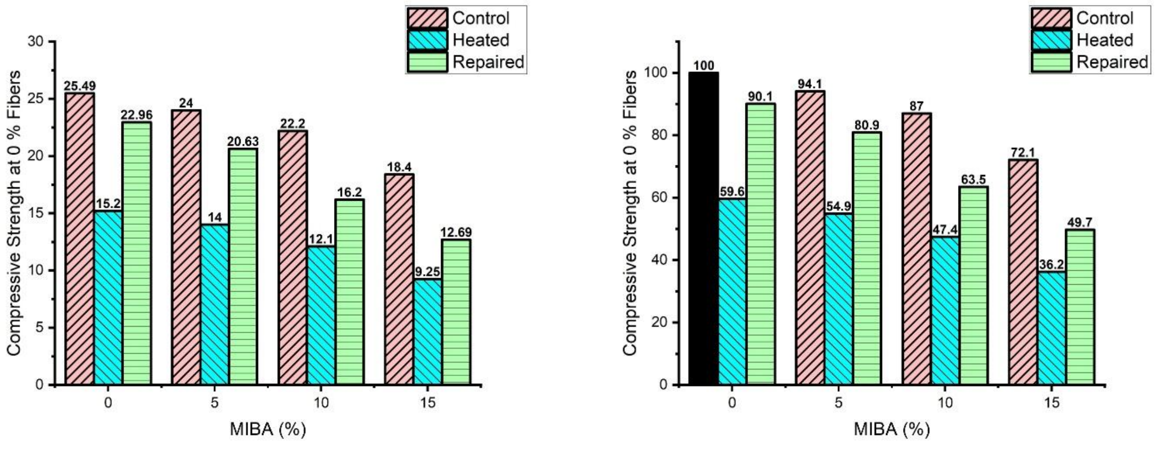

(a)

(b)

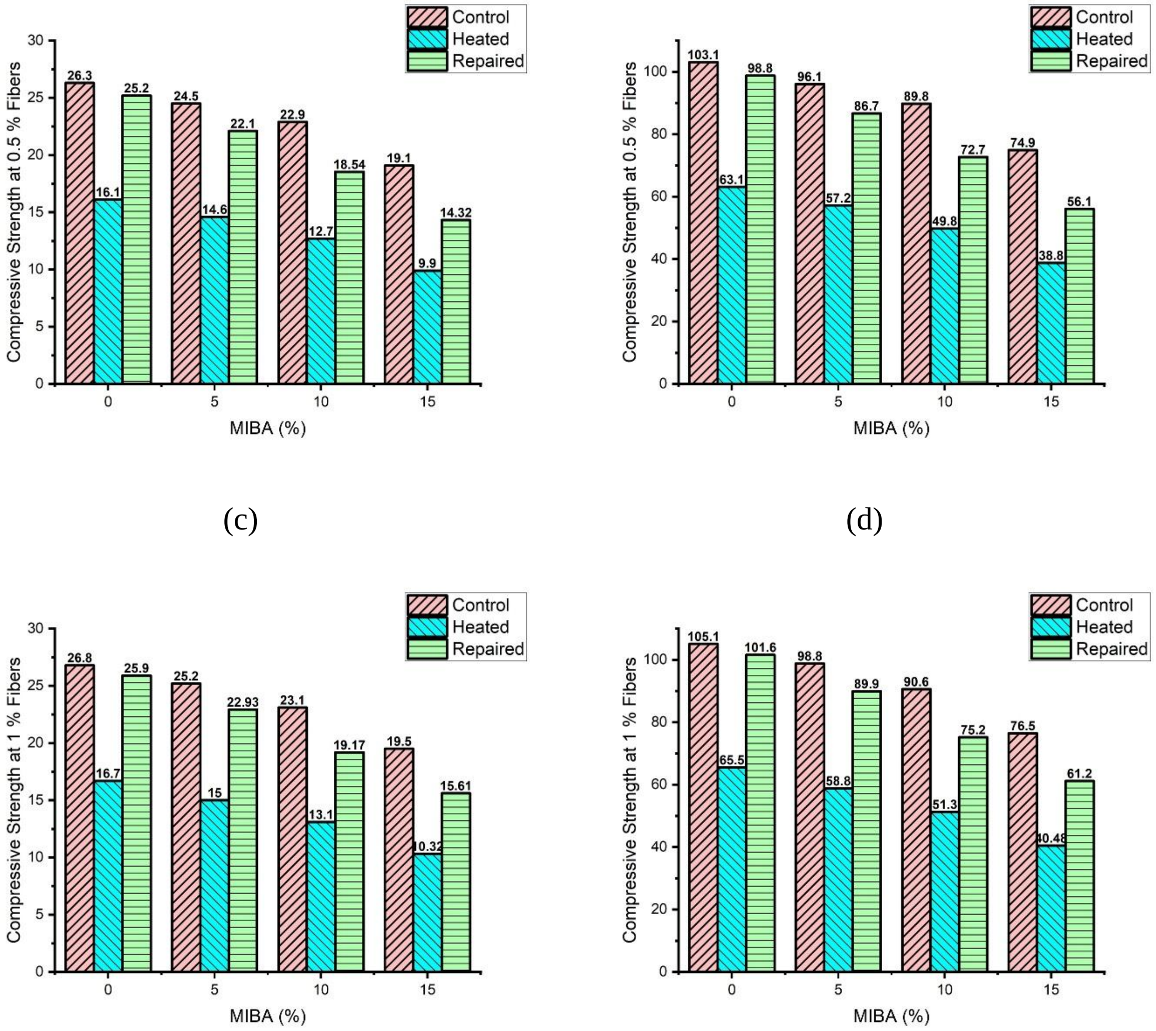

(c) (d)

(e) (f)

Figure 4-1: Effects MIBA variation on Compressive Strength

4.3 Effects of Steel Fibers on Compressive Strength

Figure 4-2 shows that at ambient conditions, steel fibers had little influence on peak compressive strength (only ±1 MPa changes at a given MIBA level), which aligns with the established view that fibers primarily enhance toughness, crack control, and post-peak behaviour rather than the elastic peak. Their effect becomes consequential once the material is thermally damaged and subsequently healed.

After exposure to 400 °C, fibers improved the retained capacity: the mean 400 °C/Control ratio increased from 0.557 (0% fibers) to 0.570 (0.5%) and 0.578 (1.0%), i.e., a 2 to 4 percentage-point gain. This improvement is attributable to crack-bridging and stress redistribution across fiber–matrix interfaces, which limits crack opening and reduces the effective loss of load-bearing area (and the risk of local spalling). After water recuring, the fiber benefit strengthened further: Healed/Control rose from 0.795 (0% fibers) to 0.855 (0.5%) and 0.877 (1.0%), reflecting 6 to 8 percentage-point higher recovery with fibers. Mechanistically, fiber-bridged cracks re-close more effectively, providing preferential pathways for water ingress and stabilising the microcrack network; both factors promote re-hydration and secondary precipitation (e.g., C-S-H/carbonates) within defects, thereby restoring stiffness and load transfer.

Notably, the relative benefit of fibers is most evident at 10–15% MIBA, where the matrix is intrinsically weaker. The crack-bridging delivers a larger proportional gain in both residual and healed strength. Taken together, these results indicate that while MIBA chiefly governs the baseline matrix quality (with a marked penalty at 15%), steel fibers govern the post-damage pathway, mitigating thermal loss and amplifying strength regain under water curing.

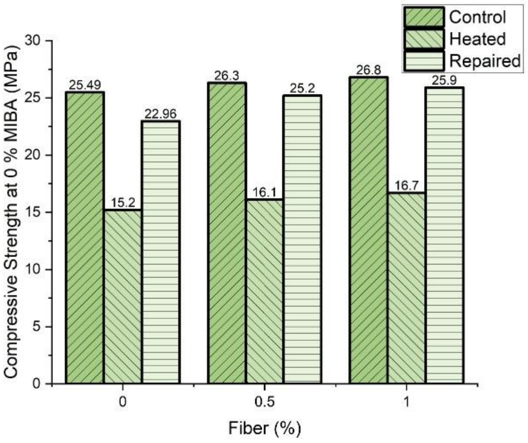

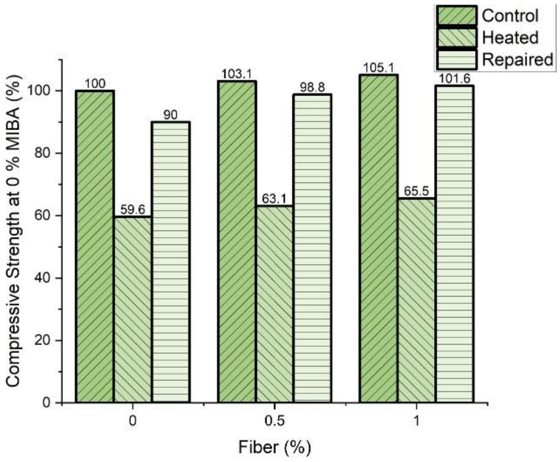

(a)

(b)

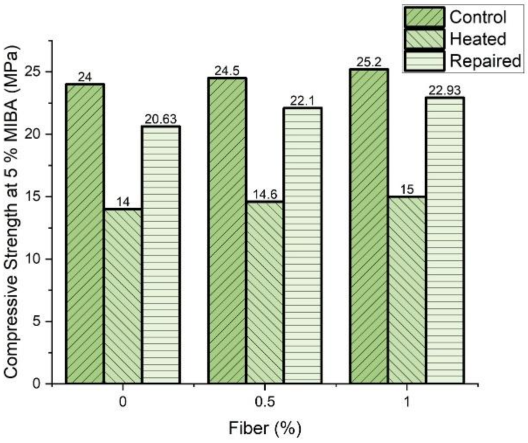
Control
Heated
Repaired
Compressive Strength at 5 % MIBA (MPa)
0
5
10
15
20
25
24
14
20.63
24.5
14.6
22.1
25.2
15
22.93
0
0.5
1
Fiber (%)

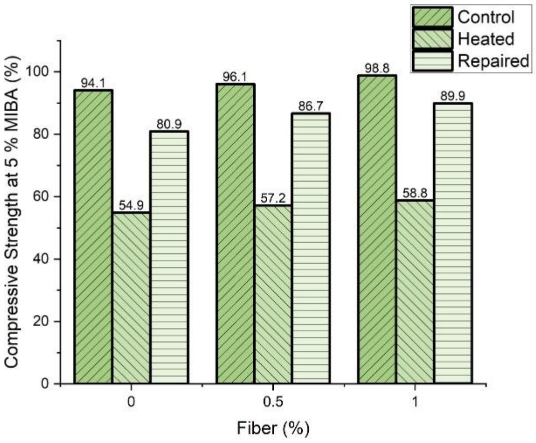
Control
Heated
Repaired
Compressive Strength at 5 % MIBA (%)
0
20
40
60
80
100
94.1
54.9
80.9
96.1
57.2
86.7
98.8
58.8
89.9
0
0.5
1
Fiber (%)

(c)

(d)

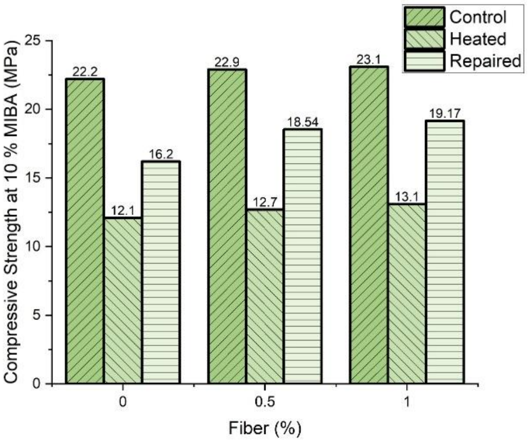
Control
Heated
Repaired
Compressive Strength at 10 % MIBA (MPa)
0
5
10
15
20
25
22.2
12.1
16.2
22.9
12.7
18.54
23.1
13.1
19.17
0
0.5
1
Fiber (%)

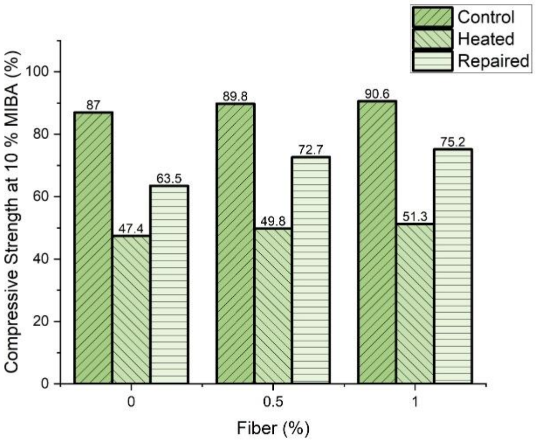
Control
Heated
Repaired
Compressive Strength at 10 % MIBA (%)
0
20
40
60
80
100
87
47.4
63.5
89.8
49.8
72.7
90.6
51.3
75.2
0
0.5
1
Fiber (%)

(e)

(f)

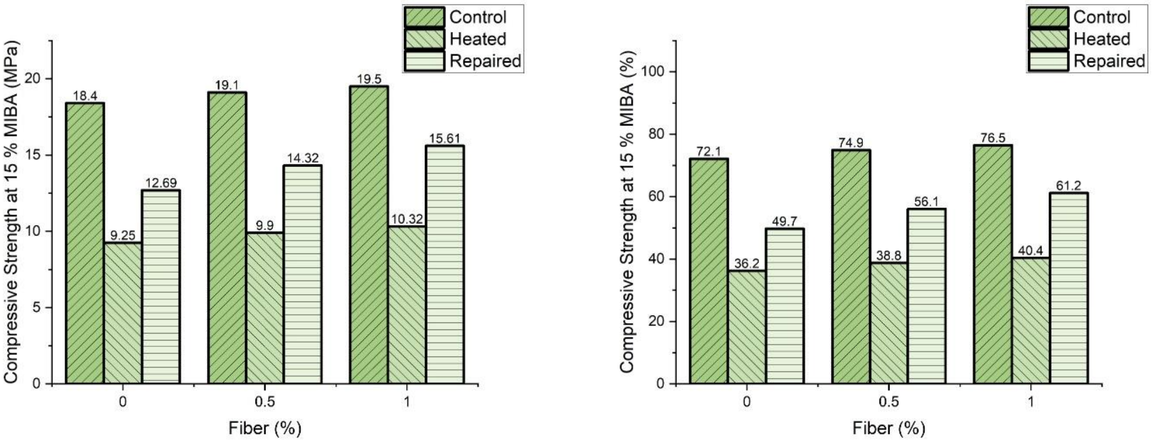

(g) (h)

Figure 4-2: Effects of Steel Fibers variation on Compressive Strength

4.4 UPV Results

Direct-path UPV through the 100-mm cube length showed a clear degradation after heating and a medium-dependent recovery thereafter. Averaged over the tested specimens, the baseline velocity prior to heating was 3.82 $\mathrm{km\cdot s^{-1}}$ (range 3.41–4.17 $\mathrm{km\cdot s^{-1}}$). Exposure to 400 °C reduced the mean to 2.02 $\mathrm{km\cdot s^{-1}}$ (range 1.38–2.49 $\mathrm{km\cdot s^{-1}}$), corresponding to an average retained ratio $V_{\text{after}} / V_{\text{before}} = 0.53$ and a damage index $DI = 1 - V_{\text{after}} / V_{\text{before}} = 0.47$.

Post-heating healing increased UPV to an overall mean of 2.79 $\mathrm{km\cdot s^{-1}}$, but the gain depended strongly on the curing medium. Specimens healed in tap water reached 3.16 $\mathrm{km\cdot s^{-1}}$ on average, whereas those kept in air reached 2.42 $\mathrm{km\cdot s^{-1}}$. Expressed as a healing index $HI = \frac{V_{heal} - V_{after}}{V_{after} - V_{before}}$ water-healed specimens recovered 0.70 (70% of the velocity lost on heating), compared with 0.15 for air-healed specimens (see

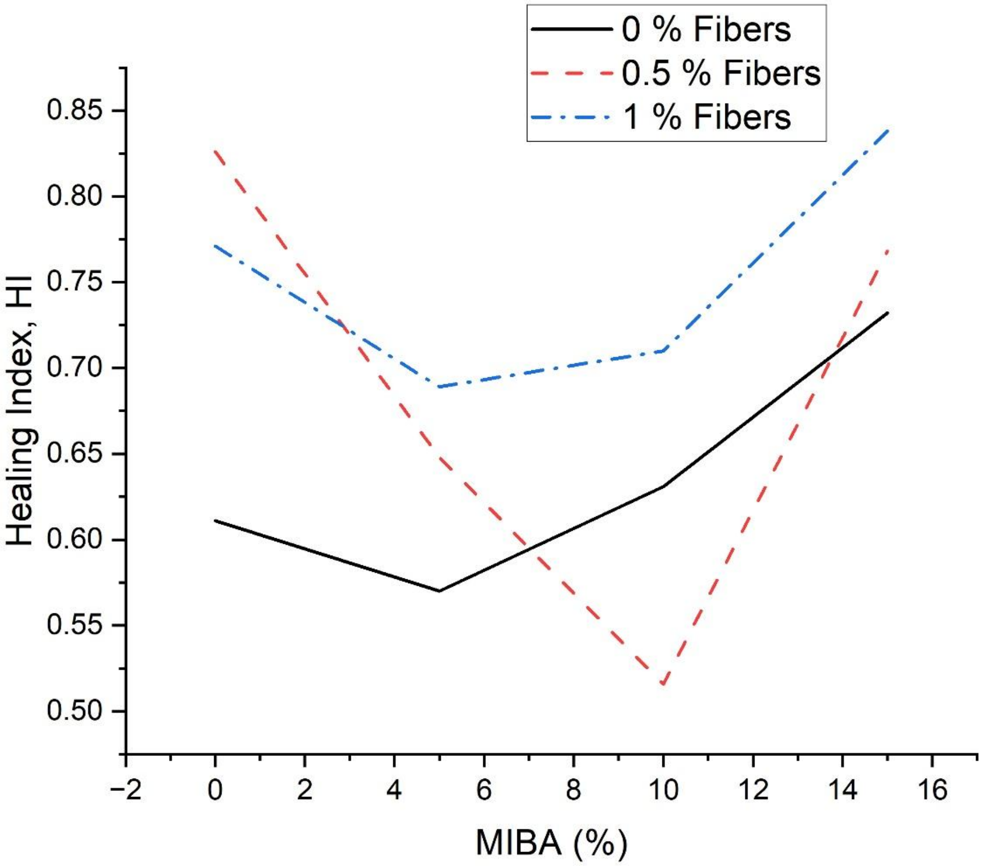

Figure 4-3). The higher recovery in water aligns with established observations for cementitious systems: moisture availability enables rehydration of unhydrated clinker and precipitation of secondary C–S–H/carbonate/silicate hydrates that bridge microcracks; in the present mixes, the inorganic granules (silicate–alkali–lime system with bentonite) plausibly supply additional ions and moisture retention, further promoting crack closure. Air curing, by contrast, limits these reactions and yields only modest UPV gains.

Trends across material factors were modest but informative. When averaged over curing medium, mixtures with 10–20% MIBA showed slightly higher pre-heating velocities (4.03 and 3.92 km·s^{-1}, respectively) than 0% and 30% MIBA (3.75 and 3.60 km·s^{-1}). After heating, all MIBA levels converged to 2.0–2.2 km·s^{-1}, indicating that the 400 °C cycle dominated over compositional differences. After healing, means clustered between 2.64–2.91 km·s^{-1} across MIBA levels (Table X), with water-healed series consistently higher than air-healed ones (see Fig. X). Steel fiber dosage had a small influence on stage means: 0.5% fibers gave the highest post-heating and post-healing averages (2.09 and 2.84 km·s^{-1}), while 1.0% fibers showed the lowest post-heating mean (1.93 km·s^{-1}), which may reflect additional fiber–matrix interfacial microcracking at elevated temperature. The details of measurements of the time travelled by the impulse through the samples is shown in Table 4-2.

Overall, UPV decreased by about 47% after the 400 °C exposure and recovered substantially under water healing but only marginally under air healing. The magnitude and direction of these changes corroborate the qualitative observations of matrix damage on heating and their partial reversal during the repair period. As UPV is a proxy for stiffness and continuity of the load path, these results anticipate the trends observed in residual and recovered mechanical performance discussed later.

Table 4-2: Ultrasonic Pulse Velocity Results

MIBA (%)	Fiber (%)	Control µs	Heated µs	Repaired µs
0	0	24.3	71.4	32.7
0	0.5	29.3	72.7	32.7
0	1	29.2	49.2	32.2
5	0	25.2	45.6	31.2
5	0.5	25.2	47.6	30.2
5	1	25.2	59.4	30.7
10	0	26.7	62.9	33.9
10	0.5	25	43.2	31.4
10	1	27.2	43.4	30.5
15	0	27.7	52.4	31.7
15	0.5	28.2	48.1	31.2
15	1	28.7	61.2	31.4

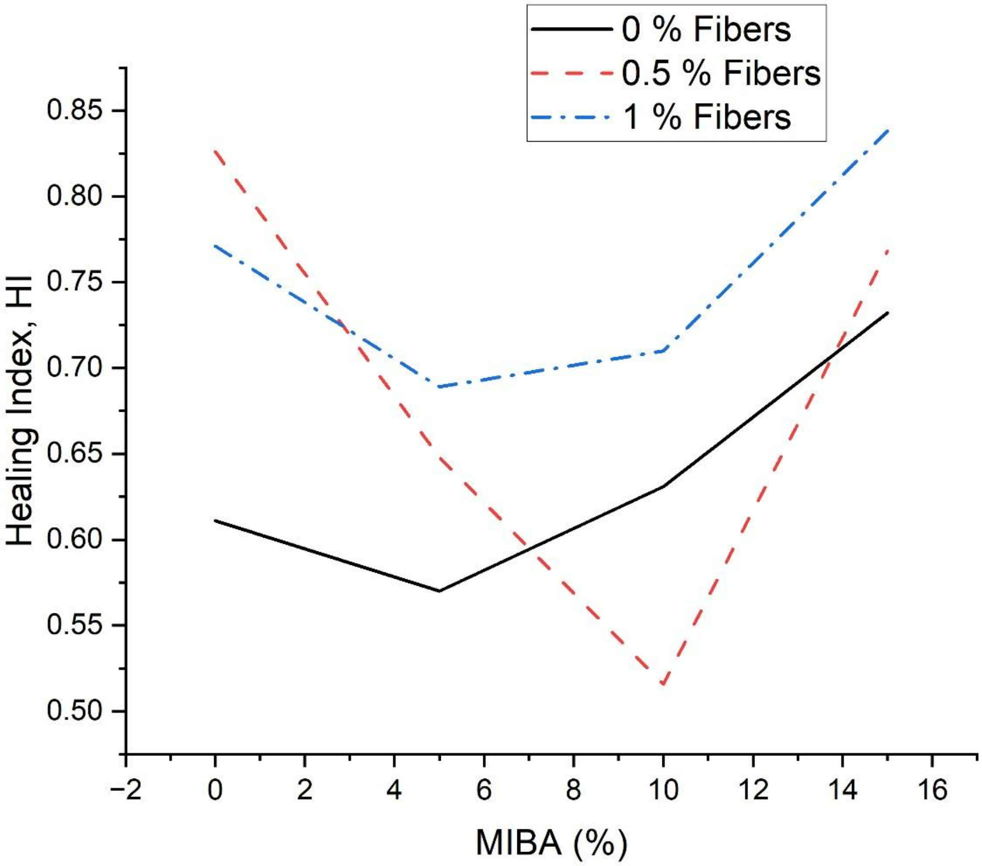

Figure 4-3: Healing index vs concentration of MIBA

4.5 Dynamic Elastic Modulus from UPV (derived results)

To obtain an independent, stiffness-based indicator of thermal damage and subsequent recovery, the longitudinal dynamic elastic modulus E_d has been estimated from the measured UPV. Using a conventional isotropic elastic relation, E_d has been computed as Equation 4-1.

$$E_d = \rho V^2 \frac{(1+\nu)(1-2\nu)}{(1-\nu)} \approx 0.9\,\rho V^2$$

Equation 4-1

$$\left(where, \quad \rho = 2400\,\frac{Kg}{m^3}, \quad \nu = 0.20\right)$$

so that the modulus has reflected the quadratic sensitivity of stiffness to wave speed. Mean wave speeds from the control, heated, and healed states have been inserted directly into this expression, and retention, damage, and healing indices have been formed to normalise the results to the control state.

The calculations have shown (refer Table 4-3) that heating to 400 °C has caused a substantial loss of dynamic stiffness: the mean modulus has fallen from 31.52 GPa at control to 8.81 GPa after heating, corresponding to a retention of 0.280 and a damage index of 0.720. This drop has indicated pervasive microcracking and paste dehydration that have coarsened the transport network and reduced the solid skeleton's effectiveness in transmitting stress. After water re-curing, the overall healed mean has risen to 16.81 GPa (retention 0.533), and the healing efficiency ηE**,** defined as the share of the heating-induced loss that has been recovered, has reached 0.352. When the healed cohort has been disaggregated by curing medium, the contrast has been pronounced: water-healed specimens have achieved 21.57 GPa (retention 0.684, $\eta E=0.562$), whereas air-healed specimens have reached only 12.65 GPa (retention 0.401, $\eta E=0.169$). These outcomes have confirmed that sustained moisture has been essential for re-hydration of unreacted clinker and for precipitation of secondary products within cracks and pores, whereas air curing has offered limited pathways for such recovery.

The stiffness-based indices have aligned with the strength-based trends reported earlier: mixes have lost a large fraction of stiffness at 400 °C and have recovered a meaningful, but incomplete, share during water exposure. Because $E_d \propto V^2$, small improvements in UPV during healing have translated into disproportionately larger gains in dynamic modulus, which has made this metric particularly sensitive to microstructural closure. Taken together, the UPV-derived moduli have provided a non-destructive, quantitative complement to compressive strength, and they have offered a practical basis for future in-situ monitoring of post-fire recovery.

Table 4-3: Dynamic modulus and indices derived from UPV

Condition	**Mean V ($\mathbf{km \cdot s^{-1}}$)**	**(E_d) (GPa)**	**Retention (E_d / $E_{d,0}$)**	**Damage index (D_E=1-E/E_0)**	**Healing Efficiency (ηE)**
Control (0)	3.82	31.52	—	—	—
Heated (H)	2.02	8.81	0.280	0.720	—
Healed (R, overall)	2.79	16.81	0.533	0.467	0.352
Healed (water only)	3.16	21.57	0.684	0.316	0.562
Healed (air only)	2.42	12.65	0.401	0.599	0.169

4.6 Factor effects and interactions (MIBA%, fiber%)

A two-factor view (MIBA replacement; steel-fiber dosage) clarifies that the baseline matrix quality is governed primarily by the ash content, while fibers matter chiefly once thermal damage and healing are involved. The experimental layout provides sufficient contrast to interpret main effects and their interaction on strength.

Increasing MIBA from 0 to 15 % produces a monotonic decline in compressive strength from 26.2 MPa to 19.0 MPa which is an absolute loss of 7.2 MPa, i.e., 27 % over the range. This shows MIBA as the dominant factor for ambient strength in this study. In practical terms, the penalty is modest up to 10 % but becomes pronounced at 15 %, where both residual capacity and subsequent healing are also depressed, consistent with clinker dilution and higher porosity at elevated replacement levels.

After 400 °C, the retained-strength ratio (Heated/Control) drops with MIBA from 0.61 (0 %) to 0.52 (15 %), an absolute decrease of 0.09 (15 % relative to the 0 % level). Following water curing, the Healed/Control ratio similarly declines from 0.94 (0 %) to 0.75 (15 %), a 0.19 absolute loss

(20 % relative). These effect sizes confirm that the ash level continues to influence performance under and after thermal distress, though the penalty is again concentrated at the upper replacement.

At ambient conditions, fibers have little influence on peak compressive strength (changes within ±1 MPa at a given MIBA level), so they are not a significant driver of the control strength in this matrix. Their role becomes consequential after heating and during healing: the 400 °C/Control ratio increases from 0.557 at 0 % fibers to 0.570 (0.5 %) and 0.578 (1.0 %), i.e., +0.013 to +0.021 in absolute terms. Under water curing, the Healed/Control ratio rises from 0.795 (0 %) to 0.855 (0.5 %) and 0.877 (1.0 %), a +0.060 to +0.082 gain. These increments, while small at ambient, are practically meaningful in the post-fire context and align with the expected crack-bridging and microcrack stabilisation provided by fibers.

The fiber benefit is most evident at higher MIBA contents (10–15 %), where the matrix is weaker; here, bridging yields a larger proportional improvement in both residual and healed strength. Conversely, at low MIBA, the baseline matrix quality is high enough that fibers contribute mainly to damage tolerance rather than the peak load. This pattern indicates a clear interaction: MIBA controls the starting point (baseline capacity), and fibers improve the trajectory after damage and during recovery.

5 CONCLUSIONS & RECOMMENDATIONS

5.1 Overview of the Study

This study evaluated the post-fire self-healing performance of concrete incorporating municipal incinerator bottom ash (MIBA), steel fibers, and fully inorganic, epoxy-coated healing granules. A 4 × 3 factorial matrix was adopted: MIBA replacement of cement at 0%, 5%, 10%, and 15% (by cement mass) crossed with steel fiber contents of 0.0%, 0.5%, and 1.0% (by volume). The water-to-binder ratio (w/b) was fixed at 0.60. The healing granules comprised sodium silicate, sodium carbonate, sodium hydroxide, calcium oxide, and bentonite (mass ratio 40:20:10:20:10), dosed at 2% of concrete mass and dispersed at batching.

Performance was examined on 100 mm cubes across three states: (i) as-cast control at 28 days, (ii) specimens heated to 400 °C at 5 $°C\cdot min^{-1}$ with a 2 h dwell followed by closed-door cooling, and (iii) specimens subjected to 28 days of water-based healing after heating. A total of 108 specimens were tested. Mechanical (compressive strength), transport (ultrasonic pulse velocity, UPV), and stiffness (dynamic modulus from UPV and density) indicators were recorded to quantify damage and recovery.

5.2 Synthesis of Key Findings

i. At ambient conditions, compressive strength decreased as MIBA content increased. The reduction was modest up to 10% replacement but became pronounced at 15%, where the cumulative penalty was on the order of one quarter relative to 0% MIBA.

ii. After heating, the residual-to-control strength ratio declined with increasing MIBA. The same trend held for the healed-to-control ratio following 28 days of water healing. In short, higher MIBA reduced both residual capacity and the ultimate recovery achievable through passive water-assisted healing.

iii. Heating to 400 °C produced limited oven-dry mass loss (1–3%) and negligible density reduction (0.98–0.99 of the control). No explosive spalling occurred under the adopted pre-drying and heating protocol, indicating that damage was governed by dehydration and microcracking rather than gross material loss.

iv. Fibers did not produce a material increase in ambient compressive strength within this matrix; however, they improved both residual capacity after heating and healing efficiency.

Gains were most visible at 10–15% MIBA, where the matrix is weaker, consistent with fiber-bridged crack control and enhanced re-closure during healing.

v. UPV dropped substantially after heating and recovered markedly under water healing, with air curing providing only modest improvement. Dynamic modulus exhibited the same pattern: a large reduction upon heating followed by significant, but incomplete, recovery in water; air curing left stiffness far below control levels. Moisture access was therefore the primary lever for microstructural recovery.

vi. MIBA primarily set the baseline matrix quality, while fibers governed the post-damage trajectory by limiting crack opening and promoting re-closure under wet curing. The relative benefit of fibers increased as MIBA content rose.

vii. The epoxy-coated, fully inorganic granules (mean diameter 8 mm) were manufactured reproducibly and dosed uniformly at concrete scale at 2% mass without mixing or placement challenges.

viii. With the present mix design and curing regime, mechanical recovery is meaningful but incomplete, while transport and stiffness indicators show larger rebounds. Water exposure is essential for effective healing; air curing alone offers limited benefit.

5.3 Conclusions

1. For the evaluated system (w/b = 0.60; untreated, sieved fine MIBA), up to 10% MIBA is a workable substitution with a manageable strength penalty. At 15% MIBA, the penalty becomes significant for both residual capacity and post-healing recovery.
2. Steel fibers in the range 0.5–1.0% by volume do not substantially increase ambient compressive strength for this matrix but do mitigate thermal damage and enhance healing, especially at higher MIBA levels.

3. Sustained water exposure after thermal damage produces pronounced recovery in UPV and dynamic modulus and improves strength to a lesser extent. Air curing yields considerably weaker recovery across all indicators.
4. Damage at 400 °C was dominated by dehydration and microcracking. The combination of pre-drying, controlled heating, and closed-door cooling avoided explosive spalling and preserved overall integrity.
5. The sodium silicate/alkali/lime/bentonite system, delivered as epoxy-coated granules and dosed at 2% of concrete mass, is compatible with conventional batching and placement.

5.4 Recommendations for Practice

1. Limit MIBA to ≤10% by cement mass in structural applications unless the strength penalty is offset via a lower w/b, supplementary cementitious materials, or targeted post-treatments. Expect a discernible decline in both residual and healed strengths at 15%.
2. Include steel fibers when fire resilience matters. Target 0.5–1.0% (vol.) to improve residual capacity and healing efficiency after moderate thermal excursions. Select hooked-end geometries and ensure adequate workability and dispersion.
3. Plan deliberate wet-curing protocols after fire**.** Where compatible with safety and durability requirements, implement 28 days of immersion or controlled wetting regimes to enable microstructural recovery. Incorporate these steps into repair method statements and acceptance criteria.
4. Use UPV-based indices to triage and verify. Establish an as-built UPV baseline. After an event, track the damage index (DI) and recovery/healing indices to decide whether to continue passive healing or to escalate to active repair measures (e.g., crack injection, overlays).

5. Pre-treat ash for higher replacement targets**.** If structural objectives require MIBA beyond 10%, implement washing/aging and, where feasible, accelerated carbonation and grinding to mitigate metallic aluminum, refine grading, and reduce transport penalties.
6. Start with the validated granule dosage. A 2% mass dosage of the inorganic granules is a practical starting point. If the w/b, MIBA level, or fiber content changes, re-validate dispersion, fresh properties, and the risk of segregation at the plant scale.

5.5 Limitations of the Study

1. A single water-to-binder ratio (0.60) was examined, with one fiber geometry and a single thermal exposure level (400 °C). Extrapolation to higher temperatures, load during heating, or member-scale behavior should be made cautiously.
2. MIBA was sieved and cleaned but not carbonated, milled, or otherwise upgraded; the results reflect that condition.
3. Healing was assessed under 28-day water immersion; wet–dry or field moisture gradients were not simulated.

5.6 Directions for Future Research

1. Re-run the matrix with pre-treated MIBA (washing + aging, accelerated carbonation, and wet grinding) to determine whether the ≤10% ceiling can be safely extended without compromising residual capacity or recovery.
2. Extend the thermal regime to 200–600 °C and include multiple heat–heal cycles to map recovery envelopes for design and maintenance planning.
3. Apply microscopy and quantitative crack-width statistics to link fiber bridging and mineral precipitate formation to measured UPV, modulus, and strength recoveries.

4. Transition to beams and slabs under realistic restraint, moisture access, and load paths. Couple UPV with load testing to establish acceptance thresholds for service reinstatement.
5. Jointly vary granule dosage and fiber content; conduct life-cycle and cost analyses to benchmark self-healing against conventional repair and retrofit strategies.

REFERENCES

Adhikary, Suman Kumar, Nikhil Rathod, Satadru Das Adhikary, Adarsh Kumar, and Priyadharshini Perumal. 2024. “Chemical-Based Self-Healing Concrete: A Review.” *Discover Civil Engineering* 1(1): 119. doi:10.1007/s44290-024-00130-7.

Amran, Mugahed, Ali M Onaizi, Roman Fediuk, Nikolai Ivanovicn Vatin, Raizal Saifulnaz Muhammad Rashid, Hakim Abdelgader, and Togay Ozbakkaloglu. 2022. “Self-Healing Concrete as a Prospective Construction Material: A Review.” *Materials (Basel, Switzerland)* 15(9). doi:10.3390/ma15093214.

Arickx, S, T Van Gerven, and C Vandecasteele. 2006. “Accelerated Carbonation for Treatment of MSWI Bottom Ash.” *Journal of Hazardous Materials* 137(1): 235–43. doi:https://doi.org/10.1016/j.jhazmat.2006.01.059.

ASTM-C138. 2023. “Standard Test Method for Density (Unit Weight), Yield, and Air Content (Gravimetric) of Concrete.”

ASTM-C143. 2015. “Standard Test Method for Slump of Hydraulic-Cement Concrete.”

ASTM-C33/C33M-18. 2018. “Standard Specification for Concrete Aggregates.” doi:10.1520/C0033_C0033M-18.

Bakker, Erwin, Henk Soen, Mark van Kempen, Ad van Leest, Gert van der Wegen, Sylvain Dehaudt, and Christopher Cheeseman. 2025. “Industrial Trials Using the Mineral Fraction of Municipal Solid Waste Incinerator Bottom Ash as a Filler in Unreinforced Concrete Products.” *Progress in Engineering Science* 2(1): 100055. doi:https://doi.org/10.1016/j.pes.2025.100055.

Bataille, Christopher G F. 2020. “Physical and Policy Pathways to Net-zero Emissions Industry.” *Wiley Interdisciplinary Reviews: Climate Change* 11(2): e633.

Beglarigale, Ahsanollah, Yoldaş Seki, Naim Yağız Demir, and Halit Yazıcı. 2018. “Sodium Silicate/Polyurethane Microcapsules Used for Self-Healing in Cementitious Materials: Monomer Optimization, Characterization, and Fracture Behavior.” *Construction and Building Materials* 162: 57–64. doi:https://doi.org/10.1016/j.conbuildmat.2017.11.164.

De Belie, Nele, Elke Gruyaert, Abir Al-Tabbaa, Paola Antonaci, Cornelia Baera, Diana Bajare, Aveline Darquennes, et al. 2018. “A Review of Self-healing Concrete for Damage Management of Structures.” *Advanced materials interfaces* 5(17): 1800074.

Beumelburg, Christoph. 2025. “World Premiere at Heidelberg Materials: Opening of CCS Facility in Norway Marks New Era of Sustainable Construction.” https://www.heidelbergmaterials.com/en/pr-2025-06-18.

CEMBUREAU. 2024. *Activity Report 2024*.

Chen, Boyu, Priyadharshini Perumal, Mirja Illikainen, and Guang Ye. 2023. “A Review on the Utilization of Municipal Solid Waste Incineration (MSWI) Bottom Ash as a Mineral Resource for Construction Materials.” *Journal of Building Engineering* 71: 106386. doi:https://doi.org/10.1016/j.jobe.2023.106386.

Chen, Boyu, Priyadharshini Perumal, Chen Liu, Yun Chen, Cheng Chang, Majda Pavlin, Davor Kvočka, et al. 2025. “Municipal Solid Waste Incineration (MSWI) Bottom Ash-Blended Cementitious Materials: Performance, Challenges, and Potential Solutions.” *Critical Reviews in Environmental Science and Technology* 55(19): 1506–33. doi:10.1080/10643389.2025.2548287.

Escoffres, P, C Desmettre, and J.-P. Charron. 2018. “Effect of a Crystalline Admixture on the Self-Healing Capability of High-Performance Fiber Reinforced Concretes in Service Conditions.” *Construction and Building Materials* 173: 763–74. doi:https://doi.org/10.1016/j.conbuildmat.2018.04.003.

Ferrara, Liberato, Visar Krelani, and Fabio Moretti. 2016. “Autogenous Healing on the Recovery of Mechanical Performance of High Performance Fibre Reinforced Cementitious Composites (HPFRCCs): Part 2 – Correlation between Healing of Mechanical Performance and Crack Sealing.” *Cement and Concrete Composites* 73: 299–315. doi:https://doi.org/10.1016/j.cemconcomp.2016.08.003.

GCCA. 2024. “Cement Industry Net Zero Progress Report 2024/25.” *Global Cement and Concrete Association (GCCA) Concrete Future*: 80.

Griffiths, Steve, Benjamin K Sovacool, Dylan D Furszyfer Del Rio, Aoife M Foley, Morgan D Bazilian, Jinsoo Kim, and Joao M Uratani. 2023. “Decarbonizing the Cement and Concrete Industry: A Systematic Review of Socio-Technical Systems, Technological Innovations, and Policy Options.” *Renewable and Sustainable Energy Reviews* 180: 113291. doi:https://doi.org/10.1016/j.rser.2023.113291.

Helal, Zinab, Hani Salim, Seleem S E Ahmad, Hesham Elemam, Ahmed I H Mohamed, and Mohamed A R Elmahdy. 2024. “Sustainable Bacteria-Based Self-Healing Steel Fiber Reinforced Concrete.” *Case Studies in Construction Materials* 20: e03389. doi:https://doi.org/10.1016/j.cscm.2024.e03389.

IEA, C S I. 2018. “Technology Roadmap Low-Carbon Transition in the Cement Industry.” *France/WBCSD, Geneva, Switzerland. IEA, Paris*.

Khoury, Gabriel Alexander. 2008. “Effect of Fire on Concrete and Concrete Structures.” *Structures Congress 2008* 2(4): 1–10. doi:10.1061/41016(314)299.

Kodur, Venkatesh. 2014. “Properties of Concrete at Elevated Temperatures.” *International Scholarly Research Notices* 2014.

Krzemień, Katarzyna, and Izabela Hager. 2015. “Post-Fire Assessment of Mechanical Properties of Concrete with the Use of the Impact-Echo Method.” *Construction and Building Materials* 96: 155–63. doi:10.1016/j.conbuildmat.2015.08.007.

Kumpueng, Park, Lalitsuda Phutthimethakul, and Nuta Supakata. 2024. “Production of Cement Mortars from Glass Powder and Municipal Incinerated Bottom Ash.” *Scientific Reports* 14(1): 1569. doi:10.1038/s41598-024-52298-8.

Lee, Kwang-Myong, Hyung-Suk Kim, Do-Keun Lee, and Kyung-Joon Shin. 2021. “Self-Healing Performance Evaluation of Concrete Incorporating Inorganic Materials Based on a Water Permeability Test.” *Materials* 14(12). doi:10.3390/ma14123202.

Li, Jinglu, Xinchun Guan, and Chenchen Zhang. 2023. “Inorganic Capsule Based on Expansive Mineral for Self-Healing Concrete.” *Cement and Concrete Composites* 144: 105305. doi:https://doi.org/10.1016/j.cemconcomp.2023.105305.

Li, Lang, Long Shi, Qingyuan Wang, Yongjie Liu, Jiangfeng Dong, Hong Zhang, and Guomin Zhang. 2020. “A Review on the Recovery of Fire-Damaged Concrete with Post-Fire-Curing.” *Construction and Building Materials* 237: 117564.

Lima, Geannina T, Laura Silvestro, Luís U Tambara Júnior, Malik Cheriaf, and Janaíde C Rocha. 2024. “Autonomous Self-Healing Agents in Cementitious Materials: Parameters and Impacts on Mortar Properties." *Buildings* 14(7). doi:10.3390/buildings14072000.

Ma, Qianmin, Rongxin Guo, Zhiman Zhao, Zhiwei Lin, and Kecheng He. 2015. "Mechanical Properties of Concrete at High Temperature — A Review." *Construction and Building Materials* 93: 371–83. doi:10.1016/j.conbuildmat.2015.05.131.

Malaiškienė, Jurgita, Edmundas Spudulis, and Rimvydas Stonys. 2023. "The Effect of Milled Municipal Solid Waste Incineration Bottom Ash on Cement Hydration and Mortar Properties." *Materials* 16(6). doi:10.3390/ma16062528.

Mario de Rooij; Kim Van Tittelboom; Nele De Belie; Erik Schlangen. 2013. "State-of-the-Art Report of RILEM Technical Committee 221-SHC: Self-Healing Phenomena in Cement-Based Materials." In *Self-Healing Phenomena in Cement-Based Materials*, doi:https://doi.org/10.1007/978-94-007-6624-2.

Noman, Muhammad, Afaq Khattak, Zeshan Alam, Muhammad Yaqub, and Ehsan Noroozinejad Farsangi. 2024. "Predicting the Residual Compressive Strength of Concrete Exposed to Elevated Temperatures Using Interpretable Machine Learning." *Practice Periodical on Structural Design and Construction* 29(4): 4024055. doi:10.1061/PPSCFX.SCENG-1536.

Noman, Muhammad, and Muhammad Yaqub. 2021. "Restoration of Dynamic Characteristics of RC T-Beams Exposed to Fire Using Post Fire Curing Technique." *Engineering Structures* 249(July 2020): 113339. doi:10.1016/j.engstruct.2021.113339.

Noman, Muhammad, Muhammad Yaqub, Muhammad Abid, Muhammad Ali Musarat, Nikolai Ivanovich Vatin, and Muhammad Usman. 2022. "Effects of Low-Cost Repair Techniques on Restoration of Mechanical Properties of Fire-Damaged Concrete." 8(January): 1–14. doi:10.3389/fmats.2021.801464.

Noman, Muhammad, Muhammad Yaqub, Muhammad Fahad, Faheem Butt, and Basit Khalid. 2022. “Dynamic Characteristics of RC Structures in Short and Long Duration Real Fires.” *Case Studies in Construction Materials* 16(February): e01058. doi:10.1016/j.cscm.2022.e01058.

Pera, J, L Coutaz, J Ambroise, and M Chababbet. 1997. “Use of Incinerator Bottom Ash in Concrete.” *Cement and Concrete Research* 27(1): 1–5. doi:https://doi.org/10.1016/S0008-8846(96)00193-7.

Phutthimethakul, Lalitsuda, and Nuta Supakata. 2022. “Partial Replacement of Municipal Incinerated Bottom Ash and PET Pellets as Fine Aggregate in Cement Mortars.” *Polymers* 14(13). doi:10.3390/polym14132597.

Qureshi, T S, A Kanellopoulos, and A Al-Tabbaa. 2016. “Encapsulation of Expansive Powder Minerals within a Concentric Glass Capsule System for Self-Healing Concrete.” *Construction and Building Materials* 121: 629–43. doi:https://doi.org/10.1016/j.conbuildmat.2016.06.030.

Roig-Flores, Marta, and Pedro Serna. 2020. “Concrete Early-Age Crack Closing by Autogenous Healing.” *Sustainability* 12(11). doi:10.3390/su12114476.

Ruane, Alexander C. 2024. “Synthesis Report of the IPCC Sixth Assessment Report (AR6).”

Scrivener, Karen, Fernando Martirena, Shashank Bishnoi, and Soumen Maity. 2018. “Calcined Clay Limestone Cements (LC3).” *Cement and Concrete Research* 114: 49–56. doi:https://doi.org/10.1016/j.cemconres.2017.08.017.

Sharma, Meenakshi, Shashank Bishnoi, Fernando Martirena, and Karen Scrivener. 2021.

“Limestone Calcined Clay Cement and Concrete: A State-of-the-Art Review.” *Cement and Concrete Research* 149: 106564. doi:https://doi.org/10.1016/j.cemconres.2021.106564.

Van Tittelboom, Kim, and Nele De Belie. 2013. “Self-Healing in Cementitious Materials—A Review.” *Materials* 6(6): 2182–2217. doi:10.3390/ma6062182.

Usman, M, M Yaqub, M Auzair, W Khaliq, M Noman, and A Afaq. 2021. “Restorability of Strength and Stiffness of Fire Damaged Concrete Using Various Composite Confinement Techniques.” *Construction and Building Materials* 272: 121984. doi:10.1016/j.conbuildmat.2020.121984.

Węgliński, Szymon, and Gabriel Martysz. 2024. “Utilization of Municipal Solid Waste Incineration Bottom Ash in Cement-Bound Mixtures.” *Sustainability* 16(5). doi:10.3390/su16051865.

Wehrung, Quentin, Davide Bernasconi, Enrico Destefanis, Caterina Caviglia, Nadia Curetti, Sara Di Felice, Erica Bicchi, Alessandro Pavese, and Linda Pastero. 2024. “Aqueous Carbonation of Waste Incineration Residues: Comparing BA, FA, and APCr Across Production Scenarios.” *Minerals* 14(12). doi:10.3390/min14121269.

Yaqub, M. 2010. “Axial Compressive and Seismic Shear Performance of Post-Heated Columns Repaired with Composite Materials Doctor of Philosophy 2010.” The University of Manchester. https://www.escholar.manchester.ac.uk/uk-ac-man-scw:101698.

Yaqub, M., C. G. Bailey, and P. Nedwell. 2011. “Axial Capacity of Post-Heated Square Columns Wrapped with FRP Composites.” *Cement and Concrete Composites* 33(6): 694–701. doi:10.1016/j.cemconcomp.2011.03.011.

Zhang, Tao, and Zengzeng Zhao. 2014. “Optimal Use of MSWI Bottom Ash in Concrete.” *International Journal of Concrete Structures and Materials* 8(2): 173–82. doi:10.1007/s40069-014-0073-4.